

# A Planning Strategy for Building a Heterogeneous Smart EM Environment

A. Benoni,<sup>(1)(2)</sup> *Member, IEEE*, M. Salucci,<sup>(1)(2)</sup> *Senior Member, IEEE*, B. Li,<sup>(3)</sup> *Member, IEEE*, and A. Massa,<sup>(1)(2)(4)(5)(6)</sup> *Fellow, IEEE*

<sup>(1)</sup> *ELEDIA Research Center (ELEDIA@UniTN - University of Trento)*

DICAM - Department of Civil, Environmental, and Mechanical Engineering

Via Mesiano 77, 38123 Trento - Italy

E-mail: {arianna.benoni, marco.salucci, andrea.massa}@unitn.it

Website: [www.eledia.org/eledia-unitn](http://www.eledia.org/eledia-unitn)

<sup>(2)</sup> *CNIT - "University of Trento" ELEDIA Research Unit*

Via Mesiano 77, 38123 Trento - Italy

E-mail: {arianna.benoni, marco.salucci, andrea.massa}@unitn.it

Website: [www.eledia.org/eledia-unitn](http://www.eledia.org/eledia-unitn)

<sup>(3)</sup> *Hangzhou Institute of Technology*

Xidian University, Hangzhou 311200 - China

E-mail: libaozhu@xidian.edu.cn

<sup>(4)</sup> *ELEDIA Research Center (ELEDIA@UESTC - UESTC)*

School of Electronic Science and Engineering, Chengdu 611731 - China

E-mail: andrea.massa@uestc.edu.cn

Website: [www.eledia.org/eledia-uestc](http://www.eledia.org/eledia-uestc)

<sup>(5)</sup> *ELEDIA Research Center (ELEDIA@TSINGHUA - Tsinghua University)*

30 Shuangqing Rd, 100084 Haidian, Beijing - China

E-mail: andrea.massa@tsinghua.edu.cn

Website: [www.eledia.org/eledia-tsinghua](http://www.eledia.org/eledia-tsinghua)

<sup>(6)</sup> *School of Electrical Engineering*

Tel Aviv University, Tel Aviv 69978 - Israel

E-mail: andrea.massa@eng.tau.ac.il

Website: <https://engineering.tau.ac.il/>

***This work has been submitted to the IEEE for possible publication. Copyright may be transferred without notice, after which this version may no longer be accessible.***

# A Planning Strategy for Building a Heterogeneous Smart EM Environment

A. Benoni, M. Salucci, B. Li, and A. Massa

## Abstract

This paper presents a planning strategy for the deployment of smart electromagnetic entities (*SEEs*) to enhance the wireless coverage and the Quality-of-Service (*QoS*) in large urban areas. The integration of different technological solutions such as integrated access-and-backhaul nodes (*IABs*), smart repeaters (*SRs*), and electromagnetic skins (*EMSs*) is here addressed to enable an effective and efficient implementation of the concept of Smart Electromagnetic Environment (*SEME*). By combining the features of such heterogeneous *SEEs* and optimizing their number, positions, orientations, and configuration, the electromagnetic (*EM*) coverage in a set of Regions-of-Interest (*RoIs*) of outdoor scenarios is recovered and/or enhanced subject to installation costs and energy consumption requirements. Numerical validations from real-world scenarios are reported to assess the effectiveness of the proposed planning scheme as well as to show the potentialities of an heterogeneous deployment of *SEMEs*.

**Key words:** Smart Electromagnetic Environment (*SEME*), Wireless Network planning, Multi-Objective Optimization (*MOP*), Static Passive *EM* Skins (*SP-EMSs*), Reconfigurable Passive *EM* Skins (*RP-EMSs*), Smart Repeaters (*SRs*), Integrated Access Backhaul Nodes (*IABs*), Metamaterials.

# 1 Introduction

Recently, both academic and industrial sectors have pushed a significant increase of the research initiatives aimed at developing new concepts and advanced wireless technologies to meet the rising demand for connectivity in existing 5G and upcoming 6G wireless networks [1]-[4]. Future wireless communication systems have to be efficient and smart enough to manage a very large data traffic for realizing the vision of a fully interconnected world also denoted as *metaverse* (*MTV*) [5]-[7]. The *MTV* is supposed to be populated by avatars of real-world items (e.g., people, vehicles, buildings, and home appliances) that collect, share, and process a massive amount of high-resolution data from the surrounding environment. Therefore, an unprecedented proliferation of new Internet-of-Everything (*IoE*) services is already ongoing, which will include extended, augmented, and virtual reality (*XR/AR/VR*) as well as telemedicine, haptics, flying vehicles, brain-computer interfaces, and connected autonomous systems. All these instances of the *MTV* require a wireless infrastructure that guarantees a low latency, a strong reliability, and high data rates to a large set of heterogeneous devices, which are simultaneously connected. In order to fulfill these requirements, the simplest and standard solutions adopted by the network operators are the installation of more base-stations (*BTSSs*), the increase of the transmitted power, and the allocation of more frequency bands. However, these recipes generally cause a significant growth of both the overall network costs and the power consumption as well as more electromagnetic (*EM*) interferences [8]. Otherwise, the concept of smart *EM* environments (*SEMEs*) is an emerging and promising alternative to effectively handling the needs of the *MTV* [9]-[13].

In a nutshell, while the propagation environment has traditionally been viewed as an obstacle to the propagation of *EM* waves, it is considered within the *SEME* framework as an additional degree-of-freedom (*DoF*) for the design of the wireless network. Although the term “*SEME*” encompasses a wide range of innovative techniques and technologies, recent efforts have mainly focused on designing cost-effective field manipulation devices (*FMDs*) and optimally planning their deployment in the propagation environment. More in detail, the use of *EMSs* [i.e., both static passive [14]-[18][19][20][56] (*SP-EMSs*) and reconfigurable passive [21]-[24][25]-[28][29] (*RP-EMSs*) - also labelled as reconfigurable intelligent surfaces (*RISs*) - electromag-

netic skins structures] has been widely investigated for enhancing the wireless coverage and the quality-of-service (*QoS*) in indoor [30]-[35] and outdoor [36]-[40] rich-scattering scenarios hosting wireless communication systems working either in the sub-6GHz [26][31][37][38] or in the millimeter-wave [11][18][41][42] frequency bands. Thanks to the capability of breaking the traditional Snell's laws [43] and the arising *EM* wave manipulation features, several proofs-of-concept have already proven the effectiveness of such material-engineered structures to successfully counteract undesired phenomena such as non-line-of-sight (*NLOS*), fading, and shadowing [37][38]. More in detail, *RP-EMSs* have garnered a significant attention in the state-of-the-art wireless literature thanks to their ability to dynamically change by using tunable components (e.g., varactor diodes [31], positive-intrinsic-negative (*PIN*) diode switches [34], graphene [44][45], and liquid crystals [29]) that in principle enable a real-time control of the reflected wave. However, *RP-EMSs* also have drawbacks compared to their static counterparts (i.e., *SP-EMSs*) such as the finite set of discrete states of the reconfigurable unit cells (*UCs*) that can limit the beamforming properties and sometimes involves the generation of unwanted beams [36]. Of course, it is possible to counteract such restrictions, but this leads to more complex *UC* layouts with higher costs and energy consumption [34]. Otherwise, *SP-EMSs* have recently emerged as a powerful and versatile technology to enhance the *EM* coverage and to improve the information transfer [20][37][38][46] with minimum costs. *SP-EMSs* comprise inexpensive elementary *UCs* (also called meta-atoms) with specific geometric and physical layouts, which are designed for yielding a controlled micro-scale wave reflection [14]. Thanks to a proper combination of these meta-atoms, *SP-EMSs* can then effectively manipulate the reflected field at a macroscopic level, while being inexpensive to fabricate and requiring no maintenance or power consumption during operation. Furthermore, the *SP-EMS* deployment does not necessitate changes to the network protocols or to the control architectures since they are virtually transparent to the upper layers (i.e., beyond the physical layer) of the communication stack.

On the other hand, the swift advancement of technologies has recently promoted the concept of a new generation of smart devices for the network infrastructure, namely smart repeaters (*SRs*) [11][47]-[50] and integrated access backhaul nodes (*IABs*) [11][50]-[52], which are able to dynamically control and redirect radio-frequency (*RF*) signals. *SRs*, also referred to as network-

controlled repeaters [53], are an evolution of the traditional *RF* repeaters used in previous wireless standards (i.e., 2G, 3G, and 4G) for enhancing the coverage offered by macro cells. They are a *non-regenerative* (i.e., they cannot decode and re-encode the received signals) type of network nodes, based on the amplify-and-forward concept, with advanced features like beam-forming operations [11][48]. On the contrary, *IABs* are *regenerative* relays wirelessly connected to the *BTS* [55] that have become a key solution for extending the coverage of 5G networks without incurring the high costs associated with the fiber deployment [52]. Towards this end, customized *IABs* planning strategies have been developed to minimize the latency, while satisfying the reliability requirement [54][56]. Moreover, some attempts of integrating *RP-EMSs* and *SRs* within *IAB* networks have been studied (e.g., [57][58]), as well.

This work deals with the implementation of a heterogeneous *SEME* based on the deployment of different types of existing *SEEs* (i.e., *SP-EMSs*, *RP-EMSs*, *SRs*, and *IABs*) in large-scale outdoor scenarios to guarantee the best trade-off between *EM* network performance (i.e., *EM* coverage and *QoS*), installation costs, and energy consumption. To the best of the authors' knowledge, the main novelties of this research work with respect to the state-of-the-art literature in the field, include (i) the development of an optimization method for enhancing the coverage in large urban outdoor scenarios thanks to the use of different *SEEs*, (ii) the definition of some guidelines for the deployment of the *SEEs*, and (iii) the introduction of a multi-objective planning strategy aimed at optimizing the wireless performance (i.e., the functional requirements) without neglecting non-functional requirements such as installation costs and energy consumption.

The paper is organized as follows. Section 2 mathematically formulates the heterogeneous planning problem (*HPP*) at hand, while the multi-objective optimization (*MOP*) solution strategy is detailed in Sect. 3. A set of representative numerical results concerned with real-world urban scenarios is reported in Sect. 4 to assess the effectiveness and to envisage the potentialities of the proposed approach in deploying next generation wireless networks. Finally, some conclusions and final remarks are drawn (Sect. 5).

## 2 Mathematical Formulation

Let us consider a large-urban scenario served by a *BTS*  $\Psi$ , located at  $\mathbf{r}_\Psi$  [ $\mathbf{r}_\Psi = (x_\Psi, y_\Psi, z_\Psi)$ ] and operating at the working frequency  $f$ , which is able to steer electronically/mechanically the radiated beam according to the spatial distribution of the users equipment (*UE*) [59][60] (Fig. 1). Moreover, the *BTS* transmits a power  $\mathcal{P}_{TX}$  and is characterized by a gain  $\mathcal{G}_\gamma$ ,  $\gamma$  being its polarization state. Due to the presence of shadowing effects as well as the *EM* scattering interactions (i.e., reflections, refractions, and diffractions) between the *BTS* and the buildings/vegetation *NLOS* conditions and multi-path phenomena generally arise so that at the  $t$ -th ( $t = 1, \dots, T$ ) time-instant there is a set of  $W$  ( $W \geq 1$ ) *RoIs*, namely the “*blind spot*” region, of extension  $\Omega(t) = \{\Omega_w(t); w = 1, \dots, W\}$  where the nominal received power,  $\mathcal{P}(\mathbf{r}, t)$ , is below the desired *QoS* threshold  $\mathcal{P}_{th}$  [i.e.,  $\mathcal{P}(\mathbf{r}, t) < \mathcal{P}_{th}$ ,  $\mathbf{r} \in \Omega(t)$ ]. In order to recover the “*coverage condition*”

$$\mathcal{P}(\mathbf{r}, t) \geq \mathcal{P}_{th} \forall \mathbf{r} \in \Omega(t), \quad (1)$$

$N$  *SEEs* belonging to an heterogeneous set of  $S$  classes [11][50] is deployed as sketched in Fig. 2. There are passive *SEEs* (*PSEs*) that only reflect the impinging *EM* field (e.g., *EMSs*), while active *SEEs* (*ASEs*) amplify and re-transmit the incoming signal (e.g., *IABs* and *SRs*). Each  $s$ -th ( $s = 1, \dots, S$ ) type of *SEE* has specific *EM* features as well as a generally different installation cost,  $\xi_s$ , and an energy consumption,  $\nu_s$ . Moreover, since the deployment of a *SEE* is not arbitrary and *ad-hoc* rules for each  $s$ -th ( $s = 1, \dots, S$ ) class of device must be fulfilled, the set of  $N$  “candidate” installation sites is *a-priori* defined by the network operator to guarantee the “feasibility” of the *SEME* implementation.

The planning problem at hand can be then stated as follows:

**Heterogeneous Planning Problem (HPP)** - Given a set of pre-defined  $N$  admissible installation sites, determine for each  $n$ -th ( $n = 1, \dots, N$ ) site the  $s$ -th ( $s = 1, \dots, S$ ) type of *SEEs* to be deployed so that the received power  $\mathcal{P}(\mathbf{r}, t)$  over  $T$  time instants in the *blind spot* region [ $\mathbf{r} \in \Omega(t)$  ( $t = 1, \dots, T$ )] fulfills the *QoS/coverage condition* (1) by minimizing the overall installation costs as well as the energy consumption.

To solve the *HPP*, a *MOP* strategy based on an integer version of the Non-Dominated Sorting Genetic Algorithm II (NSGA-II) [61] is applied as detailed in Sect. 3.

### 3 Multi-Objective Optimization Strategy

The *MOP* strategy is composed of the following building blocks (Fig. 3):

- *Site Definition (SD)* Block - This block is devoted to identify the  $N$  admissible sites where it is possible to install the  $s$ -th ( $s = 1, \dots, S$ ) type of *SEEs*;
- *SEEs Design (SEED)* Block - Starting from the knowledge of the locations of the *BTS*, the  $W$  *RoIs*, and admissible installation (i.e., building walls and poles), this block is aimed at synthesizing the complete set of *SEEs* deployable in the  $N$  candidate sites;
- *Problem Definition (PD)* Block - The objective of this block is twofold. On the one hand, it is aimed at defining the set of degrees-of-freedom (*DoFs*) that encodes a *SEME* solution of the *HPP*. On the other hand, it mathematically formulates the *HPP* as a global optimization one by defining the cost function terms to be minimized for fulfilling the problem objectives;
- *Database Computation (DC)* Block - This block is devoted to generate a database of pre-calculated coverage maps, one for each type of *SEE* deployed in an admissible site of the scenario at hand;
- *Solution Space Exploration (SSE)* Block - The last block performs an effective sampling of the solution space of the optimization problem, defined in the *PD* Block, to find an optimal Pareto front (*PF*) of *SEME* trade-off solutions.

In the following, a detailed description of each functional block is provided.

#### 3.1 SD Block

Let us assume that the  $n$ -th ( $n = 1, \dots, N$ ) site, defined by the network operator, is either a building facade, where only *EMSs* can be installed, or a pole once the “feasibility” conditions

listed in the following hold true:

### 3.1.1 EMS Deployable Region

Owing to the presence of obstacles, a direct line-of-sight (*LOS*) path between the *BTS*  $\Psi$  and a generic point  $\mathbf{r}$  of the  $w$ -th ( $w = 1, \dots, W$ ) *RoI* [ $\mathbf{r} \in \Omega_w(t)$ ] does not exist. Therefore, let us suppose that the received power in  $\mathbf{r}$  is due to a single reflection of the incident field impinging on an *EMS* placed at  $\mathbf{r}'$  [ $\mathbf{r}' = (x', y', z')$ ] when illuminated by the *BTS*. Subject to the free-space path-loss conditions, the received power in  $\mathbf{r} \in \Omega_w(t)$  ( $w = 1, \dots, W; t = 1, \dots, T$ ) exceeds the coverage threshold  $\mathcal{P}_{th}$  if the total single-hop (*BTS*  $\rightarrow$  *EMS*  $\rightarrow$  *RoI*) path length  $\mathcal{R}_w$  [Fig. 4(a)] fulfils the following inequality

$$\mathcal{R}_w \leq \frac{\lambda}{4\pi} \sqrt{\frac{\mathcal{P}_{TX} \mathcal{G}_\gamma \mathcal{G}_{RX}}{\mathcal{P}_{th}}} \quad (2)$$

where  $\lambda$  is the wavelength at  $f$  and  $\mathcal{G}_{RX}$  is the gain of the receiver, which is assumed to be an isotropic radiator (i.e.,  $\mathcal{G}_{RX} = 1$ ).

Let  $\mathbf{r}_{\Omega_w(t)}$  ( $w = 1, \dots, W; t = 1, \dots, T$ ) be the barycenter of the  $w$ -th ( $w = 1, \dots, W$ ) *RoI* at the  $t$ -th ( $t = 1, \dots, T$ ) time instant, then the average position of the  $w$ -th ( $w = 1, \dots, W$ ) *RoI* over the entire time window is given by  $\mathbf{r}_{\Omega_w} = \frac{1}{T} \sum_{t=1}^T \mathbf{r}_{\Omega_w(t)}$ . Accordingly, the condition (2) holds true only if the total path length from the *BTS* at  $\mathbf{r}_\Psi$  to the *EMS* position,  $\mathbf{r}'$ , and then to the average center of the  $w$ -th ( $w = 1, \dots, W$ ) *RoI*,  $\mathbf{r}_{\Omega_w}$ , is less than or equal to  $\mathcal{R}_w$ , that is

$$\sqrt{\sum_{u \in \{x, y, z\}} (u' - u_\Psi)^2} + \sqrt{\sum_{u \in \{x, y, z\}} (u' - u_{\Omega_w})^2} \leq \mathcal{R}_w. \quad (3)$$

The locus of points  $\mathbf{r}'$  that satisfies (3) defines the  $w$ -th ( $w = 1, \dots, W$ ) region  $\Pi_w$  that geometrically corresponds to an ellipse [Fig. 4(b)] whose two *foci* are the *BTS* position,  $\mathbf{r}_\Psi$ , and the average barycenter of the  $w$ -th ( $w = 1, \dots, W$ ) *RoI*,  $\mathbf{r}_{\Omega_w}$ .

It is worth pointing out that such a definition of  $\Pi_w$  ( $w = 1, \dots, W$ ) is done under free-space conditions ( $\epsilon_0$  and  $\mu_0$  being the free-space permittivity and permeability, respectively), thus it does not take into account the presence of the environment. To reliably handle this issue, a set of rules-of-thumbs is applied to avoid ineligible sites for the *EMSs* deployment. More

specifically, the locations in  $\Pi_w$  ( $w = 1, \dots, W$ ) that fulfil at least one of the following conditions are classified as non-admissible:

- “*Unfeasible Incident Angle*” Condition - Due to the mutual position of the *BTS*,  $\mathbf{r}_\Psi$ , and the candidate site,  $\mathbf{r}'$  ( $\mathbf{r}' \in \Pi_w$ ;  $w = 1, \dots, W$ ), the incident angle  $\theta_{inc}$  [Fig. 4(c)] is wider than the maximum physical angle for a reflection (i.e.,  $\theta_{inc} \geq 90$  [deg]);
- “*Unfeasible Reflection Angle*” Condition - Due to the position of the site,  $\mathbf{r}'$  ( $\mathbf{r}' \in \Pi_w$ ;  $w = 1, \dots, W$ ), with respect to the  $w$ -th ( $w = 1, \dots, W$ ) *RoI* center,  $\mathbf{r}_{\Omega_w}$ , the reflection angle  $\theta_{ref}$  [Fig. 4(d)] is larger than the maximum physical angle for a reflection [Fig. 4(c)] (i.e.,  $\theta_{ref} \geq 90$  [deg]);
- “*Low Incidence Power*” Condition - Due to multi-path phenomena, the incident power in  $\mathbf{r}'$  ( $\mathbf{r}' \in \Pi_w$ ;  $w = 1, \dots, W$ ) is already (i.e., before a reflection can take place) lower than the coverage threshold  $\mathcal{P}_{th}$  (i.e.,  $\mathcal{P}(\mathbf{r}', t) < \mathcal{P}_{th}$ ;  $t = 1, \dots, T$ ).

### 3.1.2 ASE Deployable Region

Dealing with *ASEs* featuring a transmitting power and a gain equal to  $\mathcal{P}_{ASE}$  and  $\mathcal{G}_{ASE}$ , respectively, only the poles locations are considered as admissible installation sites since a power source is needed. Moreover, the rooftops of the buildings are avoided since complex administrative permissions, which generally need long bureaucratic processes, are required for the deployment. Subject to these assumptions, the generic location  $\mathbf{r}'$  of the region  $\Sigma_w$  ( $w = 1, \dots, W$ ) where an *ASE* can be installed fulfils the following conditions:

- “*ASE Visibility Power*” Condition - The power received at the *ASE* location  $\mathbf{r}'$  ( $\mathbf{r}' \in \Sigma_w$ ;  $w = 1, \dots, W$ ) from the *BTS* is above the sensitivity threshold of the device,  $\mathcal{P}_\zeta$  (i.e.,  $\mathcal{P}(\mathbf{r}', t) \geq \mathcal{P}_\zeta$ ;  $t = 1, \dots, T$ );
- “*Signal Re-generation*” Condition - The re-transmitted/re-generated signal from the *ASE* located at  $\mathbf{r}'$  ( $\mathbf{r}' \in \Sigma_w$ ;  $w = 1, \dots, W$ ) reaches a target position  $\mathbf{r}$  of the  $w$ -th ( $w = 1, \dots, W$ ) *RoI*  $\Omega_w(t)$  ( $t = 1, \dots, T$ ) with a power level that ensures the fulfillment of the *QoS* requirement (i.e.,  $\mathcal{P}(\mathbf{r}, t) \geq \mathcal{P}_{th}$ ;  $t = 1, \dots, T$ ).

Thus, the generic location of an ASE,  $\mathbf{r}'$  ( $\mathbf{r}' \in \Sigma_w$ ;  $w = 1, \dots, W$ ), belongs contemporarily to two different circular regions as sketched in Fig. 5. The former region  $\Theta_\Psi$  is centered at the *BTS* position  $\mathbf{r}_\Psi$  and its radius  $\rho_\Psi$  is given by  $\rho_\Psi = \frac{\lambda}{4\pi} \sqrt{\frac{\mathcal{P}_{TX} \mathcal{G}_{TX} \mathcal{G}_{ASE}}{\mathcal{P}_\zeta}}$ . The other one,  $\Theta_{\Omega_w}$ , is centered at the *RoI* barycenter  $\mathbf{r}_{\Omega_w}$  ( $w = 1, \dots, W$ ) and has radius  $\rho_{\Omega_w}$  equal to  $\rho_{\Omega_w} = \frac{\lambda}{4\pi} \sqrt{\frac{\mathcal{P}_{ASE} \mathcal{G}_{RX} \mathcal{G}_{ASE}}{\mathcal{P}_{th}}}$ . The feasible region  $\Sigma_w$  ( $w = 1, \dots, W$ ) for an ASE deployment is then given by the intersection of those two circular regions, that is

$$\Sigma_w = \Theta_\Psi \cap \Theta_{\Omega_w}. \quad (4)$$

As in Sect. 3.1.1, the definition in (4) relies on free-space hypotheses, while (probably) some positions of the set  $\Sigma_w$  ( $w = 1, \dots, W$ ) in several real-world scenarios might not be suitable due to multipath effects or obstacles causing a signal attenuation. Therefore, as a possible countermeasure, if the actual received power at a given location  $\mathbf{r}'$  of  $\Sigma_w$  ( $w = 1, \dots, W$ ) is lower than  $\mathcal{P}_\zeta$  (i.e.,  $\mathcal{P}(\mathbf{r}', t) < \mathcal{P}_\zeta$ ;  $t = 1, \dots, T$ ), then that location is excluded from the ASE feasible deployment area.

### 3.2 SEED Block

Once the  $N$  sites for the *SEEs* installation have been selected, the design of the *SEEs* for the  $n$ -th ( $n = 1, \dots, N$ ) site is carried out by considering both passive (i.e., *EMSs*) and active (i.e., *SRs* and *IABs*) devices.

As for *EMSs*, the directions of incidence  $(\theta_{inc}^{(n)}, \varphi_{inc}^{(n)})$  and reflection  $(\theta_{ref}^{(n)}, \varphi_{ref}^{(n)})$  ( $n = 1, \dots, N$ ) of the impinging wave from the *BTS* are computed according to the approach in [37]. The *EMS* layout is then derived by following the guidelines in [14] for *SP-EMSs* and in [25] for *RP-EMSs* with a two-step synthesis procedure. In both cases, the first step consists in the computation of the “desired” electric/magnetic currents distribution on the *EMS* aperture, while the second one is devoted to determine the optimal arrangement and shaping of the *EMS* meta-atoms (*UCs*). On the one hand, a *SP-EMS* is composed of  $L$  *UCs*, realized in low-cost *PCB* technology, yielded by optimizing their  $J$  geometric descriptors so that the induced electric/magnetic currents on the *EMS* surface match the desired ones defined at the previous step of the synthesis process. On

the other hand, a *RP-EMS* is still composed of  $L$  meta-atoms, but keeping fixed the *UC* layout, while properly setting the  $B$  states of each *UC* by acting on one or more diodes/varactors to match as close as possible the “desired” surface currents.

Concerning the *ASEs* considered in this research work, *SRs* consist of two planar phased arrays of dual-polarized elements [48][53], one oriented towards the serving *BTS*  $\Psi$  and the other directed towards the  $w$ -th ( $w = 1, \dots, W$ ) *RoI*, while *IABs* are micro *BTS* modeled as a single planar phased array of dual-polarized elements and connected through in-band wireless backhaul to the *BTS* itself [55].

### 3.3 PD Block

An integer-based scheme is adopted to encode the set of *DoFs* of the *HPP* at hand so that a *SEME* solution (i.e., a solution embedding in the environment one or more types of *SEEs*) is encrypted into a  $N$ -size chromosome  $\underline{\chi}$  whose  $n$ -th ( $n = 1, \dots, N$ ) entry,  $\chi_n$ , is related to the  $n$ -th site and its integer value,  $0 \leq \chi_n \leq S$ , corresponds to the  $s$ -th ( $s = 1, \dots, S$ ) type of *SEE* deployed if  $1 \leq \chi_n \leq S$ , otherwise (i.e.,  $\chi_n = 0$ ) no *SEE* is installed in the  $n$ -th ( $n = 1, \dots, N$ ) admissible location.

Afterwards, the original *HPP* is recast as a global optimization one by defining suitable cost function terms. The first one, namely the “time-varying coverage” term  $\Phi_{CV} \{\underline{\chi}\}$ , is aimed at quantifying the average mismatch between the received power within the *blind-spot* region  $\Omega(t)$  over  $T$  time instants ( $t = 1, \dots, T$ ) when deploying the *SEME* solution encoded in  $\underline{\chi}$  and the power threshold for the *EM* coverage,  $\mathcal{P}_{th}$ . It is defined as follows

$$\Phi_{CV} \{\underline{\chi}\} \triangleq \frac{1}{T} \sum_{t=1}^T \int_{\Omega(t)} \frac{|\mathcal{P}_{th} - \mathcal{P}(\mathbf{r}, t | \underline{\chi})|}{|\mathcal{P}_{th}|} \times \mathcal{H} \{\mathcal{P}_{th} - \mathcal{P}(\mathbf{r}, t | \underline{\chi})\} d\mathbf{r} \quad (5)$$

where  $\mathcal{H} \{\circ\}$  is the Heaviside function (i.e.,  $\mathcal{H} \{\circ\} = 1$  if  $\circ \geq 0$  and  $\mathcal{H} \{\circ\} = 0$ , otherwise).

The other two terms, namely the “cost” term  $\Phi_{CS} \{\underline{\chi}\}$  and the “energy consumption” term  $\Phi_{EC} \{\underline{\chi}\}$ , quantify the installation costs and the energy consumption of the *SEME* solution  $\underline{\chi}$ ,

respectively. The former is given by

$$\Phi_{CS} \{ \underline{\chi} \} \triangleq \frac{1}{\xi_{max}} \sum_{n=1}^N \delta_{\chi_n s} \xi_s \quad (6)$$

where  $\delta_{\chi_n s}$  is the Kronecker delta (i.e.,  $\delta_{\chi_n s} = 1$  if  $\chi_n = s$  and  $\delta_{\chi_n s} = 0$  otherwise) and  $\xi_{max}$  is the maximum installation cost for deploying a feasible *SEME* solution in the  $N$  admissible sites

$$\xi_{max} = \sum_{n=1}^N \max_{s=1, \dots, S} \{ \delta_{\chi_n s} \xi_s \}. \quad (7)$$

It is worth noticing that the normalization to  $\xi_{max}$  in (6) ensures that  $\Phi_{CS}(\underline{\chi}) = 1$  when the most expensive *SEEs* are deployed in the  $N$  locations, while  $\Phi_{CS} \{ \underline{\chi} \} = 0$  when no *SEEs* are installed (i.e., the original reference situation).

Analogously, the energy term is defined as

$$\Phi_{EC} \{ \underline{\chi} \} \triangleq \frac{1}{\nu_{max}} \sum_{n=1}^N \delta_{\chi_n s} \nu_s \quad (8)$$

where  $\nu_{max} = \sum_{n=1}^N \max_{s=1, \dots, S} \{ \delta_{\chi_n s} \nu_s \}$ .

The terms in (5)-(8) model three conflicting objectives since, for instance, deploying high-performance *SEEs* generally improves the coverage, but at the expense of a higher installation cost and an increased energy usage.

### 3.4 DC Block

In order to evaluate the degree-of-optimality of a *SEME* solution,  $\underline{\chi}$ , the computation of the corresponding cost function value (i.e., the three terms  $\Phi_{CV} \{ \underline{\chi} \}$ ,  $\Phi_{CS} \{ \underline{\chi} \}$ , and  $\Phi_{EC} \{ \underline{\chi} \}$ ) is needed. Such an operation could represent one of the main computational bottlenecks in solving the *HPP* since it is generally repeated several times during the exploration of the  $N$ -dimensional solution space carried out in the *SSE* Block (Sect. 3.5). Indeed, whether the prediction of the terms (6) and (8) is immediate, since they only depend on the cost,  $\xi_s$ , and the energy consumption,  $\nu_s$ , associated to each  $s$ -th ( $s = 1, \dots, S$ ) *SEE*, the evaluation of the coverage term (5) is computationally very demanding because of the use of a *RT*-based simulation tool

to estimate the received power across  $\Omega(t)$  over  $T$  time instants ( $t = 1, \dots, T$ ). This is a heavy task mainly due to both the large size and the complex structure of the urban environment to be modeled for a faithful coverage prediction. To reduce the computational burden, the *DC* block pre-computes separately the contribution to the electric field distribution of each *SEE* when deployed in the admissible  $n$ -th ( $n = 1, \dots, N$ ) site. Then, the electric field in a generic position  $\mathbf{r}$  of  $\Omega(t)$  at the  $t$ -th ( $t = 1, \dots, T$ ) time instant generated when deploying the *SEME* devices coded by  $\underline{\chi}$  is computed as the superposition of the *EM* fields obtained by making each  $s$ -th ( $s = 1, \dots, S$ ) *SEE* in the  $n$ -th ( $n = 1, \dots, N$ ) site radiate individually

$$\mathbf{E}(\mathbf{r}, t | \underline{\chi}) = \sum_{u \in \{x, y, z\}} \sum_{n=1}^N \sum_{s=1}^S \delta_{\chi_n s} E_u^{(s, n)}(\mathbf{r}, t) \hat{\mathbf{u}} \quad (9)$$

where  $E_u^{(s, n)}(\mathbf{r}, t)$  is the  $u$ -th ( $u = \{x, y, z\}$ ) Cartesian component of the electric field generated by the  $s$ -th ( $s = 1, \dots, S$ ) *SEE* when installed in the  $n$ -th ( $n = 1, \dots, N$ ) site. Thus, the received power in  $\mathbf{r}$  ( $\mathbf{r} \in \Omega(t); t = 1, \dots, T$ ) turns out to be

$$\mathcal{P}(\mathbf{r}, t | \underline{\chi}) = \sum_{u \in \{x, y, z\}} \left\{ |E_u(\mathbf{r}, t | \underline{\chi}) + E_u^\Psi(\mathbf{r}, t)|^2 \right\} \times \frac{\lambda^2 \mathcal{G}_{RX}}{8\pi\eta_0} \quad (10)$$

where  $\eta_0$  ( $\eta_0 \triangleq \sqrt{\frac{\mu_0}{\epsilon_0}}$ ) is the free-space characteristic impedance and  $E_u^\Psi(\mathbf{r}, t)$  is the  $u$ -th ( $u = \{x, y, z\}$ ) Cartesian component of the electric field distribution generated by the *BTS* in the reference scenario without *SEEs*,  $\mathbf{E}^\Psi(\mathbf{r}, t) = \mathcal{G}(\mathbf{r}_\Psi, \mathbf{r}, t; \mathcal{P}_{TX}, \mathcal{G}_{TX})$ , which is *a-priori* estimated with a *RT*-based simulation tool.

### 3.5 SSE Block

The *HPP*, formulated in Sect. 3.3 as an optimization problem, is handled with an integer implementation of the NSGA-II [61]. Such a choice is not casual, but it is driven by the nature of the cost function at hand (i.e., multi-objective with some highly-nonlinear terms) and the type of the *DoFs* (i.e., integer variables) according to the “*No-free-lunch*” theorem for optimization [62]. Since the optimization problem at hand is inherently multi-objective with three conflicting terms, a natural solution recipe is that of defining a *PF* of non-dominated solutions, each repre-

senting a valid trade-off for the *SEME* deployment. More in detail, the *SSE* block implements the following steps:

1. *Step 0 (NSGA-II Setup)* - Select the population size  $P$  (i.e., the number of trial *SEME* solutions) and set the control parameters of the NSGA-II, namely the crossover rate,  $\kappa_c$ , the mutation rate,  $\kappa_m$ , the tourney size,  $\wp$ , and the maximum number of iterations,  $I$ ;
2. *Step 1 (Initialization)* - Reset the iteration index ( $i = 0$ ,  $i$  being the iteration index). Randomly set the initial trial solutions,  $\left\{ \underline{\chi}_i^{(p)} \right\}_{i=0} ; p = 1, \dots, P$  ( $p$  being the index of a trial *SEME* solution or “individual”) and compute the corresponding values of the cost function terms [i.e.,  $\Phi_{CV} \left\{ \underline{\chi}_i^{(p)} \right\}_{i=0}$  (5),  $\Phi_{CS} \left\{ \underline{\chi}_i^{(p)} \right\}_{i=0}$  (6), and  $\Phi_{EC} \left\{ \underline{\chi}_i^{(p)} \right\}_{i=0}$  (8)] for each  $p$ -th ( $p = 1, \dots, P$ ) individual;
3. *Step 2 (Optimization Loop)* - Update the iteration index ( $i \leftarrow i + 1$ ). Generate a new population of off-springs ( $\left\{ \tilde{\chi}_i^{(p)} ; p = 1, \dots, P \right\}$ ) by applying the genetic operators with probabilities  $\kappa_c$ ,  $\kappa_m$ , and  $\wp$  to the current population ( $\left\{ \tilde{\chi}_{i-1}^{(p)} ; p = 1, \dots, P \right\}$ ) and compute the cost functions terms  $\Phi_{CV} \left\{ \tilde{\chi}_i^{(p)} \right\}$ ,  $\Phi_{CS} \left\{ \tilde{\chi}_i^{(p)} \right\}$ , and  $\Phi_{EC} \left\{ \tilde{\chi}_i^{(p)} \right\}$  according to (5), (6), and (8). Determine the  $i$ -th *PF* of trade-off solutions,  $\left\{ \underline{\chi}_i^{(o)} ; o = 1, \dots, O \right\}$ , as the set of non-dominated solutions within the  $i$ -th offspring population. More in detail,  $\underline{\chi}_i^{(o)} = \tilde{\chi}_i^{(p)}$  if for each  $q$ -th ( $q \neq p$ ;  $q = p + 1, \dots, P$ ) individual  $\Phi_\alpha \left\{ \tilde{\chi}_i^{(p)} \right\} \leq \Phi_\alpha \left\{ \tilde{\chi}_i^{(q)} \right\}$  ( $\alpha = \{CV, CS, EC\}$ ) and it exists a cost function term  $\beta$  ( $\beta = \{CV, CS, EC\}$ ) for which  $\Phi_\beta \left\{ \tilde{\chi}_i^{(p)} \right\} \leq \Phi_\beta \left\{ \tilde{\chi}_i^{(q)} \right\}$ . If  $i < I$  then repeat “Step 2”, otherwise set  $i = I$  and goto “Step 3”;
4. *Step 3 (Output Phase)* - Output the *PF* of  $O$  non-dominated solutions,  $\left\{ \underline{\chi}_{opt}^{(o)} ; o = 1, \dots, O \right\}$ , by setting  $\underline{\chi}_{opt}^{(o)} = \underline{\chi}_i^{(o)} \Big|_{i=I}$  ( $o = 1, \dots, O$ ).

## 4 Numerical Results

The objective of this section is to assess the effectiveness and to highlight the potentialities of the proposed outdoor planning strategy. Towards this end, real-world urban scenarios have been first modeled according to the Open Street Map (*OSM*) Geographic Information System (*GIS*)

database [63] and the wireless coverage at a fixed height  $h = 1.5$  [m] has been then predicted by means of the *RT*-based simulation tool Altair WinProp [64]. More in detail, the buildings have been assumed to be made of concrete with relative permittivity  $\varepsilon_r = 4.0$  and conductivity  $\sigma = 0.01$  [S/m] [65]. Moreover, the *BTS* consisted of  $V = 3$  sectors, each  $v$ -th ( $v = 1, \dots, V$ ) one with an angular extension of  $\Delta\phi_\Psi = 120$  [deg] in azimuth and an electric down-tilt  $\Delta\vartheta_\Psi$  in elevation and composed of a rectangular array of  $Q = (13 \times 2)$   $\frac{\lambda}{2}$ -spaced slot coupled dual polarized (slant-45) square patch radiators working at  $f = 3.5$  [GHz] with a maximum gain for both polarizations of  $\mathcal{G}_\gamma = 16.3$  [dBi] ( $\gamma \in (+45, -45)$  [deg]) [37]. The *EM* behavior of such a *BTS* model has been simulated with the full-wave (*FW*) software *Ansys HFSS* [66] to take into account all the mutual coupling effects and non-idealities of the structure. Because of the symmetry of the radiators, the numerical results hereinafter are only referred to the co-polar pattern for the polarization  $\gamma = +45$ . Similar results arise when  $\gamma = -45$ .

The eco-system of  $S$  different entities [11][67][68] listed Tab. I has been considered to build the alphabet of *SEEs* to be used for synthesizing the *SEME* solutions. More in detail,

- ***SP-EMS***s have been designed according to [14] by using square-shaped meta-atoms univocally described by the side  $\ell$  of the copper metallization ( $J = 1$ ). Each *SP-EMS*  $\Gamma_{SP-EMS}$  extends on a support of area  $\Lambda$  ( $\Gamma_{SP-EMS}$ ) =  $4.58$  [m<sup>2</sup>] and it is composed of  $L = 50 \times 50$  *UCs* etched on a Rogers RT/Duroid 5870 substrate with a relative permittivity  $\varepsilon_r = 2.33$  and a tangent loss  $\tan \delta = 1.2 \times 10^{-3}$  of thickness  $\tau = 3.175$  [mm];
- ***RP-EMS***s are composed of single-bit ( $B = 1$ ) *UCs* [25] that consist of simple square patches with two edges connected to the ground plane through two *PIN* diodes and two vias circles. The reconfigurability is yielded by applying a bias voltage in the center of the patch to set both diodes either to the “ON” or to the “OFF” state. Every *RP-EMS*  $\Gamma_{RP-EMS}$  has the same area (i.e.,  $\Lambda(\Gamma_{RP-EMS}) = 4.58$  [m<sup>2</sup>]) and it includes the same number of *UCs* (i.e.,  $L = 50 \times 50$ ) of a *SP-EMS*, but it is printed on a different substrate, namely Rogers RO4350 ( $\varepsilon_r = 3.66$ ,  $\tan \delta = 4.0 \times 10^{-3}$ , and  $\tau = 1.524$  [mm]);
- ***SRs*** have been modeled according to [48] and they are composed of two identical phased arrays of  $Q = (12 \times 6)$   $\lambda/2$ -spaced slot-coupled dual-polarized (slant-45) square patches.

One array points towards the *BTS*, while the other is directed towards the *RoI*;

- *IABs* have the same structure as a *BTS*, but with lower input power for each sector [55].

The first test case deals with a urban site ( $\Xi$ ) in the north of the city of Trento (Italy) (Fig. 6). This is a commercial and industrial zone of Trento where the buildings have a height around to 10–20 [m] and there are several streets, some parks, and a railway [Fig. 6(c)]. The Google Maps satellite picture [69] and the *OSM* map [63] of such an area of extension  $\Lambda(\Xi) = 5.1 \times 10^5 \text{ [m}^2\text{]}$  are shown in Fig. 6(a) and Fig. 6(b), respectively. The *BTS* is located at the coordinates  $x_\Psi = 5.29 \times 10^2 \text{ [m]}$ ,  $y_\Psi = 4.03 \times 10^2 \text{ [m]}$ , and  $z_\Psi = 18 \text{ [m]}$  and dynamically changes the coverage, by acting on the azimuth and the down-tilt of each sector [59][60], to better serve the *UE*.

In order to illustrate the time-varying evolution,  $T = 2$  time instants have been evaluated, the details on the corresponding *BTS* coverages being reported in Tab. II. Figures 7(a)-7(b) show the power distribution computed on a grid of uniformly-spaced samples ( $\Delta x = \Delta y = 5 \text{ [m]}$  being the grid spacing) placed at a height  $h = 1.5 \text{ [m]}$ , while Fig. 7(e) points out the differences between the two time-instants. As expected, due to the presence of the environment, there are shadowing effects as well as canyoning along the streets. By setting  $\mathcal{P}_{th} = -65 \text{ [dBm]}$  [37], the thresholded versions of the coverage maps in Figs. 7(a)-7(b) turn out to be those in Figs. 7(c)-7(d) where one can identify  $W = 5$  *RoIs* with different extensions,  $\Lambda(\Omega_w(t))$  ( $w = 1, \dots, W$ ;  $t = 1, \dots, T$ ) (Tab. II). For instance, the area of the  $(w = 1)$ -th *RoI*,  $\Omega_1$ , reduces of about 13.6 % from  $\Lambda(\Omega_w(t)|_{t=1}^{w=1}) = 2750 \text{ [m}^2\text{]}$  down to  $\Lambda(\Omega_w(t)|_{t=2}^{w=1}) = 2375 \text{ [m}^2\text{]}$  due to a reconfiguration of the *BTS*. On the contrary,  $\Omega_5$  ( $w = 5$ ), slightly enlarges from  $\Lambda(\Omega_w(t)|_{t=1}^{w=5}) = 5425 \text{ [m}^2\text{]}$  up to  $\Lambda(\Omega_w(t)|_{t=2}^{w=5}) = 5450 \text{ [m}^2\text{]}$ . To recover a suitable coverage (1) within  $\Omega(t)$  ( $t = 1, \dots, T$ ), a set of  $N$  *SEEs* has been deployed by solving the *HPP* at hand by means of the *MOP* strategy in Sect. 3. Starting from the knowledge of the *BTS* and the *blind spot* region  $\Omega(t)$  ( $t = 1, \dots, T$ ), the first step was that of identifying the “candidate” sites for the *SEEs* deployment (3.1) and the  $N = 20$  locations in Fig. 8 have been selected. To illustrate the process for choosing those locations, let us detail the procedure concerned with the second ( $w = 2$ ) *RoI*,  $\Omega_2$ . Figure 9(a) shows the region  $\Pi_2$ , which has been derived according to (3) by considering a free-space path-loss. To take into account the presence of the environment, the set of rules in Sect.

3.1.1 have been applied so that some unfeasible locations [i.e., the dark-grey crosses in Fig. 9(a)] have been discarded. Similarly, Figure 9(b) shows the region  $\Sigma_2$ , determined according to the guidelines in Sect. 3.1.2, where it is possible to install an *ASE*. Successively, the complete set of  $N = 20$  *SEEs* has been off-line synthesized in the *SEED* Block (Sect. 3.2), while the full database of coverage maps has been computed in the *DC* Block (Sect. 3.4). The *HPP* has been then solved by exploring the space of admissible *SEME* solutions with the *NSGA-II* in the *SSE* Block (Sect. 3.5). Concerning the optimization loop, the control parameters have been set to  $P = 2 \times N$ ,  $I = 10^4$ ,  $\kappa_c = 0.9$ ,  $\kappa_m = 0.005$ , and  $\wp = 2$ . Moreover, the optimization has been repeated 50 times, every time with a different random seed, to assess the reliability of the solution process owing to its stochastic nature. However, since the outputted *PFs* turned out very similar, only the results of a representative run will be reported and discussed hereinafter. The evolution of the *PF* versus the iteration index  $i$  ( $i = 1, \dots, I$ ) is shown in Fig. 10. Starting from a *PF* composed of few non-dominated solutions (e.g.,  $O = 1$  when  $i = 0$ ), the *PF* becomes denser and well-distributed, by including a wide range of trade-offs between the optimization objectives, as the iterations progress until the convergence ( $i = I$ ) when  $O = 40$  non-dominated solutions belong to the *PF*. For instance, let us analyze the *SEME* solution  $\underline{\chi}^{BCS}$  that guarantees the best compromise between the three cost function terms, namely the *minimum Manhattan distance (MMD)* of the *PF* in the solution space, that is

$$\underline{\chi}^{BCS} = \arg \left[ \min_{o=1, \dots, O} (|\Phi_{CV} \{\underline{\chi}^{(o)}\}| + |\Phi_{CS} \{\underline{\chi}^{(o)}\}| + |\Phi_{EC} \{\underline{\chi}^{(o)}\}|) \right]. \quad (11)$$

Figure 11 shows  $\underline{\chi}^{BCS}$  at the representative iterations  $i = 10^2$  [Fig. 11(a)],  $i = 10^3$  [Fig. 11(b)], and  $i = I$  [Fig. 11(c)], while at the initialization ( $i = 0$ ) the only ( $O = 1$ ) solution of the *PF* is the trivial/reference one without *SEEs*.

In order to highlight the coverage improvement throughout the iterations, the evolution of the *cumulative density function (CDF)*, which is defined as

$$\mathcal{C} \left\{ \mathcal{P}(\mathbf{r}, t | \underline{\chi}) | \hat{\mathcal{P}} \right\} = \Pr \left\{ \mathcal{P}(\mathbf{r}, t | \underline{\chi}) \leq \hat{\mathcal{P}} \right\}, \quad (12)$$

is reported in Fig. 12. In (12),  $\Pr \{ \cdot \}$  denotes the probability function while  $\hat{\mathcal{P}}$  ( $\hat{\mathcal{P}} \in [-80, -30]$ )

[dBm]) is the value of received power in the blind spot region  $\Omega(t)$  at the  $t$ -th ( $t = 1, \dots, T$ ) time instant<sup>(1)</sup>. With reference to the case of  $\hat{\mathcal{P}} = \mathcal{P}_{th}$ , it turns out that there is a progressive improvement of the wireless coverage (i.e.,  $\mathcal{C} \left\{ \mathcal{P} \left( \mathbf{r}, t \left| \underline{\chi}_i^{BCS} \right|_{i=0} \right) \middle| \mathcal{P}_{th} \right\} > \mathcal{C} \left\{ \mathcal{P} \left( \mathbf{r}, t \left| \underline{\chi}_i^{BCS} \right|_{i=10^2} \right) \middle| \mathcal{P}_{th} \right\} > \mathcal{C} \left\{ \mathcal{P} \left( \mathbf{r}, t \left| \underline{\chi}_i^{BCS} \right|_{i=10^3} \right) \middle| \mathcal{P}_{th} \right\} > \mathcal{C} \left\{ \mathcal{P} \left( \mathbf{r}, t \left| \underline{\chi}_i^{BCS} \right|_{i=I} \right) \middle| \mathcal{P}_{th} \right\}$ ) starting from the reference/original scenario without *SEEs* (i.e.,  $\mathcal{C} \left\{ \mathcal{P} \left( \mathbf{r}, t \left| \underline{\chi} = 0 \right| \right) \middle| \mathcal{P}_{th} \right\} = 55.5 \%$ ) up to the convergence one (i.e.,  $\mathcal{C} \left\{ \mathcal{P} \left( \mathbf{r}, t \left| \underline{\chi}_i^{BCS} \right|_{i=I} \right) \middle| \mathcal{P}_{th} \right\} = 17.5 \%$ ) thanks to the implementation of the *SEME*.

For the sake of completeness, it is interesting to focus the attention also on other three relevant trade-off solutions besides the  $\underline{\chi}^{BCS}$  one. Namely, the “*best coverage (BC)*” *SEME* solution that yields the maximum achievable coverage,  $\underline{\chi}^{BC}$ , defined as

$$\underline{\chi}^{BC} = \arg \left[ \min_{o=1, \dots, O} \Phi_{CV} \{ \underline{\chi}^{(o)} \} \right], \quad (13)$$

the “*best trade-off coverage/cost (CC)*” solution, which is *MMD* between  $\Phi_{CV} \{ \underline{\chi} \}$  and  $\Phi_{CS} \{ \underline{\chi} \}$  by neglecting the energy consumption term, that is

$$\underline{\chi}^{CC} = \arg \left[ \min_{o=1, \dots, O} (|\Phi_{CV} \{ \underline{\chi}^{(o)} \}| + |\Phi_{CS} \{ \underline{\chi}^{(o)} \}|) \right], \quad (14)$$

and the “*best trade-off coverage/energy consumption (CE)*”, which is the *MMD* between  $\Phi_{CV} \{ \underline{\chi} \}$  and  $\Phi_{EC} \{ \underline{\chi} \}$  without taking into account the installation costs, that is

$$\underline{\chi}^{CE} = \arg \left[ \min_{o=1, \dots, O} (|\Phi_{CV} \{ \underline{\chi}^{(o)} \}| + |\Phi_{EC} \{ \underline{\chi}^{(o)} \}|) \right]. \quad (15)$$

Figure 13 shows the thresholded coverage maps at  $t = t_1$  (Fig. 13 - left column) and  $t = t_2$  (Fig. 13 - right column) together with the *SEEs* deployment dictated by  $\underline{\chi}^{BC}$  [Figs. 13(a)-13(b)],  $\underline{\chi}^{BCS}$  [Figs. 13(c)-13(d)],  $\underline{\chi}^{CC}$  [Figs. 13(e)-13(f)], and  $\underline{\chi}^{CE}$  [Figs. 13(g)-13(h)], while a quantitative comparison among those *PF* solutions is summarized in Tab. IV. As expected, the *BC* solution requires the installation of more *ASEs* (i.e., 2 *IABs* and 1 *SR*) to yield the complete restoration of the optimal coverage in all  $W = 5$  *RoIs* [Fig. 13(a)], but it turns out to be the most “impactful” one in terms of installation costs ( $\xi^{BC} = 18000$  [\$]) and energy consumption

<sup>(1)</sup>Since the *CDF* plots are very similar, only the result for  $t = t_1$  is shown.

( $\nu^{BC} = 720$  [W]). Otherwise,  $\underline{\chi}^{BCS}$  [Figs. 13(c)-13(d)] is the optimal trade-off between the three conflicting objectives that reaches an average reduction of the blind-spot area  $\Omega(t)$  equal to  $\Delta\Omega^{BCS}(t_1) = 86.1\%$  and  $\Delta\Omega^{BCS}(t_2) = 88.9\%$  [ $\Delta\Omega(t) \triangleq \frac{\Lambda(\Omega(t)|_{\underline{\chi}=0}) - \Lambda(\Omega(t)|_{\underline{\chi}})}{\Lambda(\Omega_w(t)|_{\underline{\chi}=0})} \times 100$ ] by installing 6 *SP-EMSs*, 1 *RP-EMSs*, and 3 *SRs* (Tab. IV). On the other hand, to minimize the installation costs, while maximizing the coverage, the solution  $\underline{\chi}^{CC}$  [Figs. 13(e)-13(f)] selects *SP-EMSs* instead of *RP-EMSs* and only one *SR* has been installed (Tab. IV). However, the *QoS* enhancement is not so relevant since the reduction of  $\Omega_5$  ( $w = 5$ ) is  $\Lambda(\Omega_w(t)|_{t=1}^{w=5}) \approx 55\%$  and  $\Lambda(\Omega_w(t)|_{t=1}^{w=5}) \approx 50\%$ . Conversely,  $\underline{\chi}^{CE}$  encodes a *SEME* solution with 1 *SR* and 19 *EMSs* (i.e., 15 *SP-EMSs* and 4 *RP-EMSs*) (Tab. IV) that guarantees a better coverage in all the *RoIs* [Figs. 13(g)-13(h)] with a reduction of  $\Omega(t)$  of  $\Delta\Omega^{CE}(t_1) \approx 76\%$  and  $\Delta\Omega^{CE}(t_2) \approx 80\%$ . All these outcomes are confirmed and highlighted both pictorially, by the difference maps ( $\Delta\mathcal{P}(\mathbf{r}, t) \triangleq \mathcal{P}(\mathbf{r}, t|_{\underline{\chi}=0}) - \mathcal{P}(\mathbf{r}, t|_{\underline{\chi}^\beta})$ ,  $\beta \in \{BC, BCS, CC, CE\}$ ) in Fig. 14, and quantitatively through the statistics of the coverage improvement in Tab. V. Moreover, Figure 15 shows the behaviour of the *CDF* of the received power in  $\Omega(t)$  at the time-instants  $t_1$  [Fig. 15(a)] and  $t_2$  [Fig. 15(b)]. Obviously,  $\mathcal{C}\{\mathcal{P}(\mathbf{r}, t|_{\underline{\chi}^{BC}})|\mathcal{P}_{th}\} = 0\%$  whatever the time instant ( $t = 1, \dots, T$ ), but let us analyze the other most representative *PF* solutions that take into account the installation costs and the energy consumption, as well. It turns out that  $\mathcal{C}\{\mathcal{P}(\mathbf{r}, t_1|_{\underline{\chi}^{BCS}})|\mathcal{P}_{th}\} = 7.8\%$  vs.  $\mathcal{C}\{\mathcal{P}(\mathbf{r}, t_1|_{\underline{\chi}^{CC}})|\mathcal{P}_{th}\} = 18.5\%$  and  $\mathcal{C}\{\mathcal{P}(\mathbf{r}, t_1|_{\underline{\chi}^{CE}})|\mathcal{P}_{th}\} = 13.5\%$  [Fig. 15(a)] as well as  $\mathcal{C}\{\mathcal{P}(\mathbf{r}, t_2|_{\underline{\chi}^{BCS}})|\mathcal{P}_{th}\} = 5.8\%$  vs.  $\mathcal{C}\{\mathcal{P}(\mathbf{r}, t_2|_{\underline{\chi}^{CC}})|\mathcal{P}_{th}\} = 18.3\%$ , and  $\mathcal{C}\{\mathcal{P}(\mathbf{r}, t_2|_{\underline{\chi}^{CE}})|\mathcal{P}_{th}\} = 10.6\%$  [Fig. 15(b)]. Finally, it is worth pointing out that an improvement similar to that yielded with the *SEME* implementation coded into  $\underline{\chi}^{BCS}$  can be obtained without a *SEME* infrastructure by increasing the input power of the *BTS* by the 525% at  $t_1$  (Fig. 15(a):  $\mathcal{P}_{TX} = 20$  [W]  $\rightarrow$   $\mathcal{P}_{TX} = 125$  [W]) and 550% at  $t_2$  (Fig. 15(b):  $\mathcal{P}_{TX} = 20$  [W]  $\rightarrow$   $\mathcal{P}_{TX} = 130$  [W]).

The second benchmark is concerned with a residential scenario featuring a higher density of buildings. More specifically, the area has a surface of  $\Lambda(\Xi) = 500 \times 500$  [m<sup>2</sup>] and is located in the “San Martino” district of the city of Trento (Italy) (Fig. 16). Still keeping a  $V = 3$ -sectors *BTS* reconfigurable over  $T = 2$  time instants, the behavior and the characteristics of the *BTS* are summarized in Tab. VI, while the nominal/reference coverage maps are shown in

Fig. 17 where  $W = 7$  RoIs are present. According to the guidelines in Sect. 3.1,  $N = 25$  sites have been determined (Fig. 18) of which 19 locations are reserved to EMSs, while the remaining 6 sites are suitable for all kind of SEEs. Despite the wider search space, which amounts to  $1.8 \times 10^{13}$  SEEs configurations, the MOP converged after  $I$  iterations to the PF given in Fig. 19 where the solutions  $\underline{\chi}^{BC}$  [Figs. 20(a)-20(b) and Tab. VII],  $\underline{\chi}^{BCS}$  [Figs. 20(c)-20(d) and Tab. VII],  $\underline{\chi}^{CC}$  [Figs. 20(e)-20(f) and Tab. VII], and  $\underline{\chi}^{CE}$  [Figs. 20(g)-20(h) and Tab. VII] are highlighted. As for the EM coverages, Table VIII gives the statistics of the difference map  $\Delta\mathcal{P}(\mathbf{r}, t)$  ( $t = 1, \dots, T$ ) together with the percentage of reduction of each  $w$ -th ( $w = 1, \dots, W$ ) RoI defined as  $\Delta\Omega_w(t) \triangleq \frac{\Lambda(\Omega_w(t)|\underline{\chi}=0) - \Lambda(\Omega_w(t)|\underline{\chi})}{\Lambda(\Omega_w(t)|\underline{\chi}=0)}$ . For completeness, Figure 20 shows the thresholded coverage maps at the time instants  $t_1$  (Fig. 20 - left column) and  $t_2$  (Fig. 20 - right column), while Figure 21 compares the CDFs. Once again, the solution  $\underline{\chi}^{BC}$  always yields the full coverage in the whole blind-spot area,  $\{\Omega(t); t = 1, \dots, T\}$ , while the second best coverage SEEs deployment,  $\underline{\chi}^{BCS}$ , reaches a probability that a UE receives a power level below the threshold  $\mathcal{P}_{th}$  around 5 % (i.e.,  $\mathcal{C}\{\mathcal{P}(\mathbf{r}, t_1 | \underline{\chi}^{BCS}) | \mathcal{P}_{th}\} = 4.9\%$  and  $\mathcal{C}\{\mathcal{P}(\mathbf{r}, t_1 | \underline{\chi}^{BCS}) | \mathcal{P}_{th}\} = 5.3\%$ ).

The final experiment has been devoted to analyze the impact on the coverage of using active and/or passive SEEs. Towards this end, Figure 22 splits the contributions of each device of the best compromise solution,  $\underline{\chi}^{BCS}$ . More in detail, the blue line is related to the deployment of one IAB and 3 SRs, while the orange line is concerned with the case where only EMSs are mounted on the building facades. As expected, ASEs strongly contribute to the improvement of the QoS. However, the statistics of the difference maps in Tab. IX point out the relevance of EMSs. For instance, the region  $\Omega_5$  ( $w = 5$ ) reduces by an amount of  $\Delta\Omega_5(t_1) = 78.3\%$  and  $\Delta\Omega_5(t_2) = 92.8\%$  thanks to both active and passive SEEs, while it turns out that  $\Delta\Omega_5(t_1) = 43.5\%$  and  $\Delta\Omega_5(t_2) = 28.6\%$  deploying only ASEs. On the contrary, the coverage enhancement in the region  $w = 7$  due to EMSs is limited to  $\Delta\Omega_7(t_1) = 10.1\%$  and  $\Delta\Omega_7(t_2) = 12.7\%$ , while the presence of a SR in the neighbourhood of the RoI allows one to achieve  $\Delta\Omega_7(t_1) = 71.9\%$  and  $\Delta\Omega_7(t_2) = 74.6\%$ . These outcomes, even though circumscribed to the EM coverage, further point out the need, for a network planner, to evaluate the benefits of both active and passive devices to build effective and reliable SEMEs in large urban areas.

## 5 Conclusions

The *HPP* has been addressed to fulfill *QoS* requirements in large urban scenarios, while reducing the installation costs and the energy consumption. An innovative *MOP* strategy has been proposed to determine the setup of the problem *DoFs*, namely the positions and the type of the deployable *SEEs*. Such an approach makes available to the network operator a *PF* that comprises several trade-off solutions among which he can select the most suitable one. Numerical results, concerned with real-world scenarios, have been reported to assess the effectiveness of the proposed planning method. Effective *SEEs* deployments have been obtained when considering different typologies of urban scenarios (e.g., industrial and residential) further pointing out the capabilities as well as the flexibility of the *MOP*-based approach.

Future works, beyond the scope of this paper, will be aimed at extending the proposed approach (a) to different scenarios (e.g., indoor) and *EM* sources (e.g., *Wi-Fi* access points) by also introducing (b) the management of multi-hop (*MH*) links between different kinds of *SEEs*, and (c) alternative definitions of the cost function to take into account other/complementary system requirements (e.g., capacity-driven optimization).

## Acknowledgements

This work benefited from the networking activities carried out within the Project Project “AURORA - Smart Materials for Ubiquitous Energy Harvesting, Storage, and Delivery in Next Generation Sustainable Environments” funded by the Italian Ministry for Universities and Research within the PRIN-PNRR 2022 Program (CUP: E53D23014760001), the Project DICAM-EXC funded by the Italian Ministry of Education, Universities and Research (MUR) (Departments of Excellence 2023-2027, grant L232/2016), and the Project Partnership on Telecommunications of the Future (PE000000001 - program RESTART), funded by the European Union under the Italian National Recovery and Resilience Plan (NRRP) of NextGenerationEU (CUP: E63C22002040007). A. Massa wishes to thank E. Vico and L. Massa for the never-ending inspiration, support, guidance, and help.

## References

- [1] H. Tataria, M. Shafi, A. F. Molisch, M. Dohler, H. Sjoland, and F. Tufvesson, "6G wireless systems: vision, requirements, challenges, insights, and opportunities," *Proc. IEEE*, vol. 109, no. 7, pp. 1166-1199, Jul. 2021.
- [2] W. Jiang, B. Han, M. A. Habibi, and H. D. Schotten, "The road towards 6G: a comprehensive survey," *IEEE Open J. Commun. Soc.*, vol. 2, pp. 334-366, 2021.
- [3] C. Wang, P. Zhang, N. Kumar, L. Liu, and T. Yang, "GCWCN: 6G-based global coverage wireless communication network architecture," *IEEE Network*, vol. 37, no. 3, pp. 218-223, May 2023.
- [4] L. Chiaraviglio, C. Di Paolo, and N. Blefari-Melazzi, "5G network planning under service and EMF constraints: Formulation and solutions," *IEEE Trans. Mobile Comput.*, vol. 21, no. 9, pp. 3053-3070, Sep. 2022.
- [5] Z. Zhang, Y. Zhou, L. Teng, W. Sun, C. Li, X. Ming, Z.-P. Zhang, and G. Zhai, "Quality-of-experience evaluation for digital twins in 6G network environments," *IEEE Trans. Broadcast.*, 2024 (DOI: 10.1109/TBC.2023.3345656).
- [6] T. Q. Duong, D. Van Huynh, S. R. Khosravirad, V. Sharma, O. A. Dobre, and H. Shin, "From digital twin to metaverse: the role of 6G ultrareliable and low-latency communications with multi-tier computing," *IEEE Wireless Commun.*, vol. 30, no. 3, pp. 140-146, Jun. 2023.
- [7] N. A. Mitsiou, V. K. Papanikolaou, P. D. Diamantoulakis, T. Q. Duong, and G. K. Karagiannidis, "Digital twin-aided orchestration of mobile edge computing with grant-free access," *IEEE Open J. Commun. Soc.*, vol. 4, pp. 841-853, 2023.
- [8] A. Puglielli *et al.*, "Design of energy- and cost-efficient massive MIMO arrays," *IEEE Proc.*, vol. 104, no. 3, pp. 586-606, Mar. 2016.

- [9] A. Massa, A. Benoni, P. Da Ru, S. K. Goudos, B. Li, G. Oliveri, A. Polo, P. Rocca, and M. Salucci, "Designing smart electromagnetic environments for next-generation wireless communications," *Telecom*, vol. 2, no. 2, pp. 213-221, May 2021.
- [10] M. Di Renzo, A. Zappone, M. Debbah, M.-S. Alouini, C. Yuen, J. de Rosny, and S. Tretyakov, "Smart radio environments empowered by reconfigurable intelligent surfaces: How it works, state of research, and the road ahead," *IEEE J. Sel. Areas Commun.*, vol. 38, no. 11, pp. 2450-2525, Nov. 2020.
- [11] R. Flamini, D. De Donno, J. Gambini, F. Giuppi, C. Mazzucco, A. Milani, and L. Resteghini, "Towards a heterogeneous smart electromagnetic environment for millimeter-wave communications: an industrial viewpoint," *IEEE Trans. Antennas Propag.*, vol. 70, no. 10, pp. 8898-8910, Oct. 2022.
- [12] F. Yang, D. Erricolo, and A. Massa, "Guest Editorial Smart Electromagnetic Environment," *IEEE Trans. Antennas Propag.*, vol. 70, no. 10, pp. 8687-8690, Oct. 2022.
- [13] R. Liu, Q. Wu, M. Di Renzo, and Y. Yuan, "A path to smart radio environments: an industrial viewpoint on reconfigurable intelligent surfaces," *IEEE Wireless Commun.*, vol. 29, no. 1, pp. 202-208, Feb. 2022.
- [14] G. Oliveri, P. Rocca, M. Salucci, and A. Massa, "Holographic smart EM skins for advanced beam power shaping in next generation wireless environments," *IEEE J. Multiscale Multiphys. Comput. Tech.*, vol. 6, pp. 171-182, Oct. 2021.
- [15] A. Diaz-Rubio and S. A. Tretyakov, "Macroscopic modeling of anomalously reflecting metasurfaces: angular response and far-field scattering," *IEEE Trans. Antennas Propag.*, vol. 69, no. 10, pp. 6560-6571, Oct. 2021.
- [16] G. Oliveri, F. Zardi, P. Rocca, M. Salucci, and A. Massa, "Building a smart EM environment - AI-enhanced aperiodic micro-scale design of passive EM skins," *IEEE Trans. Antennas Propag.*, vol. 70, no. 10, pp. 8757-8770, Oct. 2022.
- [17] G. Oliveri, F. Zardi, P. Rocca, M. Salucci, and A. Massa, "Constrained design of passive static EM skins," *IEEE Trans. Antennas Propag.*, vol. 71, no. 2, pp. 1528-1538, Feb. 2023.

- [18] P. Rocca, P. Da Ru, N. Anselmi, M. Salucci, G. Oliveri, D. Erricolo, and A. Massa, "On the design of modular reflecting EM skins for enhanced urban wireless coverage," *IEEE Trans. Antennas Propag.*, vol. 70, no. 10, pp. 8771-8784, Oct. 2022.
- [19] C. Yepes, M. Faenzi, S. Maci, and E. Martini, "Perfect non-specular reflection with polarization control by using a locally passive metasurface sheet on a grounded dielectric slab," *Appl. Phys. Lett.*, vol. 118, no. 23, Jun. 2021.
- [20] A. Freni, M. Beccaria, A. Mazzinghi, A. Massaccesi, and P. Pirinoli, "Low-profile and low-visual impact smart electromagnetic curved passive skins for enhancing connectivity in urban scenarios," *Electronics*, vol. 12, no. 21, p. 4491, Nov. 2023.
- [21] V. Degli-Esposti, E. M. Vitucci, M. D. Renzo, and S. A. Tretyakov, "Reradiation and scattering from a reconfigurable intelligent surface: a general macroscopic model," *IEEE Trans. Antennas Propag.*, vol. 70, no. 10, pp. 8691-8706, Oct. 2022.
- [22] J. C. Liang, Q. Cheng, Y. Gao, C. Xiao, S. Gao, L. Zhang, S. Jin, and T. J. Cui, "An angle-insensitive 3-bit reconfigurable intelligent surface," *IEEE Trans. Antennas Propag.*, vol. 70, no. 10, pp. 8798-8808, Oct. 2022.
- [23] P. Mei, Y. Cai, K. Zhao, Z. Ying, G. F. Pedersen, X. Q. Lin, and S. Zhang, "On the study of reconfigurable intelligent surfaces in the near-field region," *IEEE Trans. Antennas Propag.*, vol. 70, no. 10, pp. 8718-8728, Oct. 2022.
- [24] Z. Zhang, J. W. Zhang, J. W. Wu, J. C. Liang, Z. X. Wang, Q. Cheng, Q. S. Cheng, T. J. Cui, H. Q. Yang, G. B. Liu, and S. R. Wang, "Macromodeling of reconfigurable intelligent surface based on microwave network theory," *IEEE Trans. Antennas Propag.*, vol. 70, no. 10, pp. 8707-8717, Oct. 2022.
- [25] G. Oliveri, P. Rocca, M. Salucci, D. Erricolo, and A. Massa, "Multi-scale single-bit RP-EMS synthesis for advanced propagation manipulation through system-by-design," *IEEE Trans. Antennas Propag.*, vol. 70, no. 10, pp. 8809-8824, Oct. 2022.

- [26] R. Wang, Y. Yang, B. Makki, and A. Shamim, "A wideband reconfigurable intelligent surface for 5G millimeter-wave applications," *IEEE Trans. Antennas Propag.*, vol. 72, no. 3, pp. 2399-2410, Mar. 2024.
- [27] M. Barbuto, Z. Hamzavi-Zarghani, M. Longhi, A. Monti, D. Ramaccia, S. Vellucci, A. Toscano, and F. Bilotti, "Metasurfaces 3.0: a new paradigm for enabling smart electromagnetic environments," *IEEE Trans. Antennas Propag.*, vol. 70, no. 10, pp. 8883-8897, Oct. 2022.
- [28] L. Stefanini, D. Ramaccia, M. Barbuto, Z. Hamzavi-Zarghani, M. Longhi, A. Monti, S. Vellucci, A. Toscano, and F. Bilotti, "A statistical approach for robust metasurfaces and metasurface-based RIS engineering," *IEEE Trans. Antennas Propag.*, vol. 72, no. 6, pp. 5402-5407, Jun. 2024.
- [29] X. Li, H. Sato, H. Fujikake, and Q. Chen, "Development of two-dimensional steerable reflectarray with liquid crystal for reconfigurable intelligent surface applications," *IEEE Trans. Antennas Propag.*, vol. 72, no. 3, pp. 2108-2123, Mar. 2024.
- [30] A. Benoni, F. Capra, M. Salucci, and A. Massa, "Toward real-world indoor smart electromagnetic environments - A large-scale experimental demonstration," *IEEE Trans. Antennas Propag.*, vol. 71, no. 11, pp. 8450-8463, Nov. 2023.
- [31] A. Araghi, M. Khalily, M. Safaei, A. Bagheri, V. Singh, F. Wang, and R. Tafazolli, "Reconfigurable intelligent surface (RIS) in the sub-6 GHz band: design, implementation, and real-world demonstration," *IEEE Access*, vol. 10, pp. 2646-2655, Jan. 2022.
- [32] S. Kayraklik, I. Yildirim, Y. Gevez, E. Basar, and A. Gorcin, "Indoor coverage enhancement for RIS-assisted communication systems: Practical measurements and efficient grouping," *ICC 2023 - IEEE Int. Conf. Commun.*, Rome, Italy, May 2023, pp. 485-490.
- [33] M. Lodro, J.-B. Gros, S. Greedy, G. Lerosey, A. Al Rawi, and G. Gradoni, "Experimental evaluation of multi-operator RIS-assisted links in indoor environment," arXiv:2206.07788 [eess.SP], Jun. 2022.

- [34] J. Rains, J. Kazim, A. Tukmanov, T. J. Cui, L. Zhang, Q. H. Abbasi, and M. A. Imran, "High-resolution programmable scattering for wireless coverage enhancement: an indoor field trial campaign," *IEEE Trans. Antennas Propag.*, vol. 71, no. 1, pp. 518-530, Jan. 2023.
- [35] L. Dai, B. Wang, M. Wang, X. Yang, J. Tan, S. Bi, S. Xu, F. Yang, Z. Chen, M. D. Renzo, C.-B. Chae, and L. Hanzo, "Reconfigurable intelligent surface-based wireless communications: antenna design, prototyping, and experimental results," *IEEE Access*, vol. 8, pp. 45913-45923, Mar. 2020.
- [36] X. Pei, H. Yin, L. Tan, L. Cao, Z. Li, K. Wang, K. Zhang, and E. Bjornson, "RIS-Aided wireless communications: prototyping, adaptive beamforming, and indoor/outdoor field trials," *IEEE Trans. Commun.*, vol. 69, no. 12, pp. 8627- 8640, Dec. 2021.
- [37] A. Benoni, M. Salucci, G. Oliveri, P. Rocca, B. Li, and A. Massa, "Planning of EM skins for improved quality-of-service in urban areas," *IEEE Trans. Antennas Propag.*, vol. 70, no. 10, pp. 8849-8862, Oct. 2022.
- [38] M. Salucci, A. Benoni, G. Oliveri, P. Rocca, B. Li, and A. Massa, "A multi-hop strategy for the planning of EM skins in a smart electromagnetic environment," *IEEE Trans. Antennas Propag.*, vol. 71, no. 3, pp. 2758-2767, Mar. 2023.
- [39] J. Sang, Y. Yuan, W. Tang, Y. Li, X. Li, S. Jin, Q. Cheng, and T. J. Cui, "Coverage enhancement by deploying RIS in 5G commercial mobile networks: Field trials," *IEEE Trans. Wireless Commun.*, vol. 31, no. 1, pp. 172-180, Feb. 2024.
- [40] G. C. Trichopoulos, P. Theofanopoulos, B. Kashyap, A. Shekhawat, A. Modi, T. Osman, S. Kumar, A. Sengar, A. Chang, and A. Alkhateeb, "Design and evaluation of reconfigurable intelligent surfaces in real-world environment," *IEEE Open J. Commun. Soc.*, vol. 3, pp. 462-474, 2022.
- [41] W. Tang, X. Chen, M. Z. Chen, J. Y. Dai, Y. Han, M. Di Renzo, S. Jin, Q. Cheng, and T. J. Cui, "Path loss modeling and measurements for reconfigurable intelligent surfaces in the

- millimeter-wave frequency band," *IEEE Trans. Commun.*, vol. 70, no. 9, pp. 6259-6276, Sep. 2022.
- [42] R. Wang, Y. Yang, B. Makki, and A. Shamim, "A wideband reconfigurable intelligent surface for 5G millimeter-wave applications," *IEEE Trans. Antennas Propag.*, vol. 72, no. 3, pp. 2399-2410, Mar. 2024.
- [43] G. Oliveri, M. Salucci, and A. Massa, "Generalized analysis and unified design of EM skins," *IEEE Trans. Antennas Propag.*, vol. 71, no. 8, pp. 6579-6592, Aug. 2023.
- [44] S. Dash, C. Psomas, I. Krikidis, I. F. Akyildiz, and A. Pitsillides, "Active control of THz waves in wireless environments using graphene-based RIS," *IEEE Trans. Antennas Propag.*, vol. 70, no. 10, pp. 8785-8797, Oct. 2022.
- [45] J. Lee, H. Seo, and W. Choi, "Computation-efficient reflection coefficient design for graphene-based RIS in wireless communications," *IEEE Trans. Veh. Technol.*, vol. 73, no. 3, pp. 3663-3677, Mar. 2024.
- [46] S. Hager, K. Heimann, S. Bocker, and C. Wietfeld, "Holistic enlightening of blackspots with passive tailorable reflecting surfaces for efficient urban mmWave networks," *IEEE Access*, vol. 11, pp. 39318-39332, 2023.
- [47] J. Romeu, S. Blanch, L. Pradell, A. Barlabé, J. -M. Rius, M. Albert-Gali, L. Jofre-Roca, C. Mazzucco, and R. Flamini, "Lens based switched beam antenna for a 5G smart repeater," *IEEE Antennas Wireless Propag. Lett.*, vol. 22, no. 10, pp. 2482-2486, Oct. 2023.
- [48] R. A. Ayoubi, M. Mizmizi, D. Tagliaferri, D. De Donno, and U. Spagnolini, "Network-controlled repeaters vs. reconfigurable intelligent surfaces for 6G mmW coverage extension: a simulative comparison," *2023 21st Mediterranean Communication and Computer Networking Conference (MedComNet)*, Island of Ponza, Italy, 2023, pp. 196-202.
- [49] S. Vellucci, A. Monti, M. Barbuto, Z. Hamzavi-Zarghani, M. Longhi, D. Ramaccia, L. Stefanini, A. Toscano, and F. Bilotti, "Metasurface coatings enabling antenna reconfigurability for next-generation communications smart repeaters," *2023 27th International*

*Congress on Artificial Materials for Novel Wave Phenomena (Metamaterials)*, Chania, Greece, 2023, pp. X-405-X-407.

- [50] C. -K. Wen, L. -S. Tsai, A. Shojaeifard, P. -K. Liao, K. -K. Wong, and C. -B. Chae, "Shaping a smarter electromagnetic landscape: IAB, NCR, and RIS in 5G standard and future 6G," *IEEE Commun. Standards Mag.*, vol. 8, no. 1, pp. 72-78, Mar. 2024.
- [51] X. Jia, P. Deng, L. Yang, and H. Zhu, "Spectrum and energy efficiencies for multiuser pairs massive MIMO systems with full-duplex amplify-and-forward relay," *IEEE Access*, vol. 3, pp. 1907-1918, Oct. 2015.
- [52] C. Madapatha, B. Makki, C. Fang, O. Teyeb, E. Dahlman, M.-S. Alouini, and T. Svensson, "On integrated access and backhaul networks: current status and potentials," *IEEE Open J. Commun. Soc.*, vol. 1, pp. 1374-1389, 2020.
- [53] 3GPP, "5G; NR repeater radio transmission and reception," *Tech. Rep.*, Release 17, TS 38.106, v. 17.1.0, 2022-08.
- [54] H. Yin, S. Roy, and L. Cao, "Routing and resource allocation for IAB multi-hop network in 5G advanced," *IEEE Trans. Commun.*, vol. 70, no. 10, pp. 6704-6717, Oct. 2022.
- [55] 3GPP, "5G; NR integrated access and backhaul (IAB) radio transmission and reception," *Tech. Rep.*, Release 16, TS 38.174, v. 16.2.0, 2021-04.
- [56] L. Li, Y. Li, S. K. Bose, and G. Shen, "Topology planning using Q-learning for microwave-based wireless backhaul networks," *IEEE Trans. Cogn. Commun. Netw.*, vol. 9, no. 4, pp. 1041-1052, Aug. 2023.
- [57] P. Fiore, E. Moro, I. Filippini, A. Capone, and D. D. Donno, "Boosting 5G mm-wave IAB reliability with reconfigurable intelligent surfaces," *2022 IEEE Wirel. Commun. Netw. Conf. (WCNC)*, Austin, TX, USA, pp. 758-763, 2022.
- [58] G. Leone, E. Moro, I. Filippini, A. Capone, and D. D. Donno, "Towards reliable mmWave 6G RAN: Reconfigurable surfaces, smart repeaters, or both?," *2022 20th International*

*Symposium on Modeling and Optimization in Mobile, Ad hoc, and Wireless Networks (WiOpt)*, Torino, Italy, pp. 81-88, 2022.

- [59] F. Kasem, A. Haskou, and Z. Dawy, "On antenna parameters self optimization in LTE cellular networks," *2013 Third Int. Conf. Commun. Inf. Technol. (ICCIT)*, Beirut, Lebanon, Jun. 2013, pp. 44-48.
- [60] Y. You and D. Kolokotronis, "Dynamic antenna azimuth planning for 3G, 4G and future 5G broadband radio networks", *ISWCS Workshop on Ultra-Dense Cell-Less 5G Cellular Networks: Wireless Access and Programmable Network Architecture (5G Cell-Less Nets) (ISWCS)*, Bologna, Italy, Aug. 2017.
- [61] K. Deb, A. Pratap, S. Agarwal, and T. Meyarivan, "A fast and elitist multiobjective genetic algorithm: NSGA-II," *IEEE Trans. Evol. Comput.*, vol. 6, no. 2, pp. 182-197, Apr. 2002.
- [62] D. H. Wolpert and W. G. Macready, "No free lunch theorems for optimization," *IEEE Trans. Evol. Computat.*, vol. 1, no. 1, pp. 67-82, Apr. 1997.
- [63] OpenStreetMap. Accessed on: June 26, 2024. [Online]. Available: <https://www.openstreetmap.org/>
- [64] Altair Winprop 2021, Altair Engineering, Inc., [www.altairhyperworks.com/feko](http://www.altairhyperworks.com/feko).
- [65] D. J. Daniels, *Ground Penetrating Radar* (2nd Ed.), London, UK: The Institution of Electrical Engineers, 2004.
- [66] ANSYS Electromagnetics Suite - HFSS (2021). ANSYS, Inc.
- [67] *Data Sheet CEL-FI GO G51 5G Dual Band Cellular Mobile Phone Repeater*. Accessed on: Jun. 2024. [Online] Available: <https://tincan.solutions/media/wysiwyg/pdf/products/celfi/Cel-Fi-GO-G51-Datasheet.pdf>
- [68] M. Polese, M. Giordani, T. Zugno, A. Roy, S. Goyal, D. Castor, and M. Zorzi, "Integrated access and backhaul in 5G mmwave networks: potential and challenges," *IEEE Commun. Mag.*, vol. 58, no. 3, pp. 62-68, Mar. 2020.

[69] Google, Google Maps. Accessed on: Jun. 2024 [Online]. Available:  
<https://www.google.com/maps>

## FIGURE CAPTIONS

- **Figure 1.** Sketch of an urban time-varying scenario at different time instants: (a)  $t_1$  and (b)  $t_2$ .
- **Figure 2.** Sketch of an heterogeneous *SEME*.
- **Figure 3.** Block diagram of the *MOP* strategy.
- **Figure 4.** *EMS Deployable Region* - Sketch of (a) the single-hop path length,  $\mathcal{R}_w$ , (b) the  $w$ -th ( $w = 1, \dots, W$ ) region  $\Pi_w$ , (c) the “*Unfeasible Incident Angle*” Condition, and (d) the “*Unfeasible Reflection Angle*” Condition.
- **Figure 5.** *ASE Deployable Region* - Sketch of the  $w$ -th ( $w = 1, \dots, W$ ) region  $\Sigma_w$ .
- **Figure 6.** *Numerical Assessment (Test Case 1 - “Trento Nord”;  $f = 3.5$  [GHz])* - Pictures of (a) the Google Map screenshot, (b) the corresponding *OSM* cartography, and (c) its “*Urban Vegetation-Building Mask*”.
- **Figure 7.** *Numerical Assessment (Test Case 1 - “Trento Nord”;  $f = 3.5$  [GHz])* - Pictures of (a)(b) the reference/nominal power distribution,  $\{\mathcal{P}(\mathbf{r}, t); \mathbf{r} \in \Xi\}$ , (c)(d) the corresponding thresholded coverage map ( $\mathcal{P}_{th} = -65$  [dBm]) at the time instant (a)(c)  $t_1$  and (b)(d)  $t_2$  together with (e) the time-difference power map ( $|\Delta\mathcal{P}(\mathbf{r})| = |\mathcal{P}(\mathbf{r}, t_2) - \mathcal{P}(\mathbf{r}, t_1)|; \mathbf{r} \in \Xi$ ).
- **Figure 8.** *Numerical Assessment (Test Case 1 - “Trento Nord”;  $f = 3.5$  [GHz])* - Sketch of the “*candidate*” sites for *SEEs* deployment.
- **Figure 9.** *Numerical Assessment (Test Case 1 - “Trento Nord”;  $f = 3.5$  [GHz])* - Sketch of (a) the *EMS Deployable Region*,  $\Pi_2$ , and (b) the *ASE Deployable Region*,  $\Sigma_2$ , with the locations of the “*feasible/unfeasible*” installation sites.
- **Figure 10.** *Numerical Assessment (Test Case 1 - “Trento Nord”;  $f = 3.5$  [GHz])* - Plot of the evolution of the *PF* evolution during the iterative process ( $i$  being the iteration index) and representative points in the multi-objective cost function space of the set of “*relevant*” trade-off solutions,  $\{\underline{\chi}^{BC}, \underline{\chi}^{BCS}, \underline{\chi}^{CC}, \underline{\chi}^{CE}\}$ , at the convergence ( $i = I$ ).

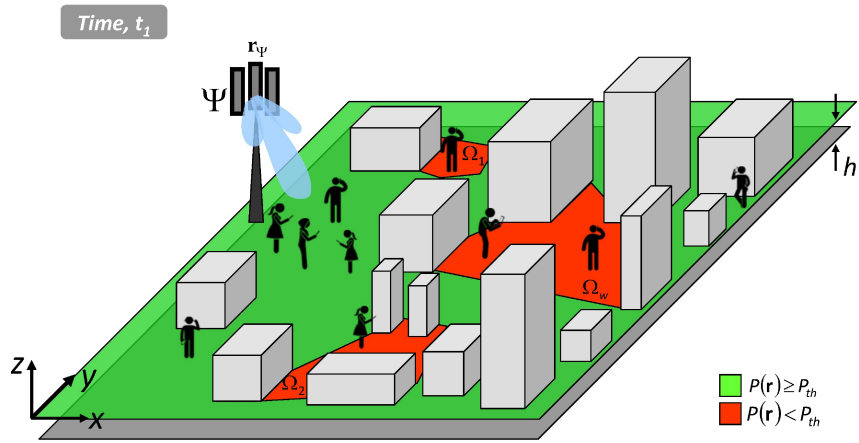
- **Figure 11.** *Numerical Assessment (Test Case 1 - “Trento Nord”;  $f = 3.5$  [GHz])* - Sketch of the *SEEs* deployment coded into  $\underline{\chi}_i^{BCS}$  at the  $i$ -th iteration: (a)  $i = 10^2$ , (b)  $i = 10^3$ , and (c)  $i = I$  (convergence iteration).
- **Figure 12.** *Numerical Assessment (Test Case 1 - “Trento Nord”;  $f = 3.5$  [GHz])* - Plot of the iterative evolution of the *CDF* of the received power,  $\mathcal{P}(\mathbf{r}, t)$ , within the *blind-spot* region,  $\mathbf{r} \in \Omega(t)$ , at the  $t$ -th ( $t = 1$ ) time-instant,  $t_1$ , in correspondence with the *SEEs* deployment coded into  $\underline{\chi}_i^{BCS}$  ( $i$  being the iteration index).
- **Figure 13.** *Numerical Assessment (Test Case 1 - “Trento Nord”;  $f = 3.5$  [GHz])* - Pictures of the thresholded coverage map ( $\mathcal{P}_{th} = -65$  [dBm]) at the time instant (a)(c)(e)(g)  $t_1$  and (b)(d)(f)(h)  $t_2$  yielded by deploying the *SEEs* configuration coded into (a)(b)  $\underline{\chi}^{BC}$ , (c)(d)  $\underline{\chi}^{BCS}$ , (e)(f)  $\underline{\chi}^{CC}$ , and (g)(h)  $\underline{\chi}^{CE}$ .
- **Figure 14.** *Numerical Assessment (Test Case 1 - “Trento Nord”;  $f = 3.5$  [GHz])* - Pictures of the difference coverage map,  $\{\Delta\mathcal{P}(\mathbf{r}, t); \mathbf{r} \in \Xi\}$  [ $\Delta\mathcal{P}(\mathbf{r}, t) \triangleq \mathcal{P}(\mathbf{r}, t | \underline{\chi} = 0) - \mathcal{P}(\mathbf{r}, t | \underline{\chi}^\beta)$ ], at the time instant (a)(c)(e)(g)  $t = t_1$  and (b)(d)(f)(h)  $t = t_2$  yielded by deploying the *SEEs* configuration coded into  $\underline{\chi}^\beta$ : (a)(b)  $\beta = BC$ , (c)(d)  $\beta = BCS$ , (e)(f)  $\beta = CC$ , and (g)(h)  $\beta = CE$ .
- **Figure 15.** *Numerical Assessment (Test Case 1 - “Trento Nord”;  $f = 3.5$  [GHz])* - Plots of the *CDF* of the received power,  $\mathcal{P}(\mathbf{r}, t)$ , within the *blind-spot* region,  $\mathbf{r} \in \Omega(t)$ , at the time-instant (a)  $t_1$  and (b)  $t_2$ .
- **Figure 16.** *Numerical Assessment (Test Case 2 - “San Martino”;  $f = 3.5$  [GHz])* - Pictures of (a) the Google Map screenshot, (b) the corresponding *OSM* cartography, and (c) its “Urban Vegetation-Building Mask”.
- **Figure 17.** *Numerical Assessment (Test Case 2 - “San Martino”;  $f = 3.5$  [GHz])* - Maps of (a)(b) the reference/nominal power distribution,  $\{\mathcal{P}(\mathbf{r}, t); \mathbf{r} \in \Xi\}$ , (c)(d) the corresponding thresholded coverage map ( $\mathcal{P}_{th} = -65$  [dBm]) at the time instant (a)(c)  $t_1$  and (b)(d)  $t_2$  together with (e) the time-difference power map ( $|\Delta\mathcal{P}(\mathbf{r})| = |\mathcal{P}(\mathbf{r}, t_2) - \mathcal{P}(\mathbf{r}, t_1)|; \mathbf{r} \in \Xi$ ).

- **Figure 18.** *Numerical Assessment (Test Case 2 - “San Martino”;  $f = 3.5$  [GHz])* - Sketch of the “candidate” sites for *SEEs* deployment.
- **Figure 19.** *Numerical Assessment (Test Case 2 - “San Martino”;  $f = 3.5$  [GHz])* - Plot of the *PF* at the convergence iteration ( $i = I$ ) with the representative points in the multi-objective cost function space of the set of “relevant” trade-off solutions,  $\{\underline{\chi}^{BC}, \underline{\chi}^{BCS}, \underline{\chi}^{CC}, \underline{\chi}^{CE}\}$ .
- **Figure 20.** *Numerical Assessment (Test Case 2 - “San Martino”;  $f = 3.5$  [GHz])* - Pictures of the thresholded coverage map ( $\mathcal{P}_{th} = -65$  [dBm]) at the time instant (a)(c)(e)(g)  $t_1$  and (b)(d)(f)(h)  $t_2$  yielded by deploying the *SEEs* configuration coded into (a)(b)  $\underline{\chi}^{BC}$ , (c)(d)  $\underline{\chi}^{BCS}$ , (e)(f)  $\underline{\chi}^{CC}$ , and (g)(h)  $\underline{\chi}^{CE}$ .
- **Figure 21.** *Numerical Assessment (Test Case 2 - “San Martino”;  $f = 3.5$  [GHz])* - Plots of the *CDF* of the received power,  $\mathcal{P}(\mathbf{r}, t)$ , within the *blind-spot* region,  $\mathbf{r} \in \Omega(t)$ , at the time-instant (a)  $t_1$  and (b)  $t_2$ .
- **Figure 22.** *Numerical Assessment (Test Case 2 - “San Martino”;  $f = 3.5$  [GHz])* - Plots of the *CDF* of the received power,  $\mathcal{P}(\mathbf{r}, t)$ , within the *blind-spot* region,  $\mathbf{r} \in \Omega(t)$ , at the time-instant (a)  $t_1$  and (b)  $t_2$ .

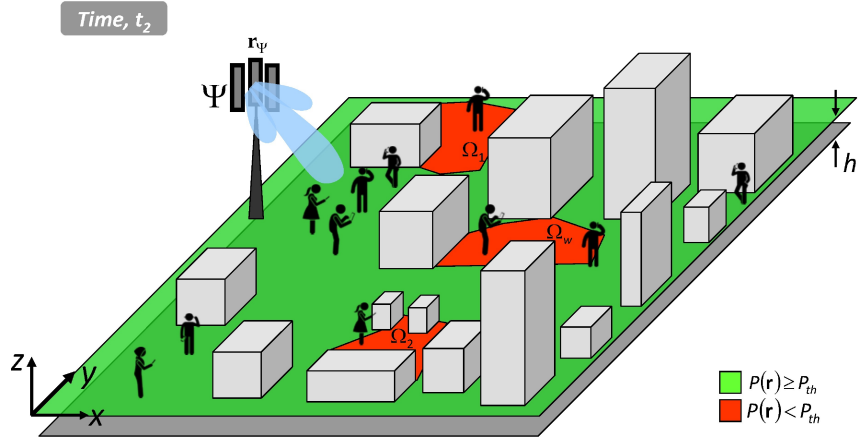
## TABLE CAPTIONS

- **Table I.** Smart entities (*SEEs*).
- **Table II.** *Numerical Assessment (Test Case 1 - “Trento Nord”;  $f = 3.5$  [GHz])* - *BTS* radiation features.
- **Table III.** *Numerical Assessment (Test Case 1 - “Trento Nord”;  $f = 3.5$  [GHz])* - *RoIs* extensions.
- **Table IV.** *Numerical Assessment (Test Case 1 - “Trento Nord”;  $f = 3.5$  [GHz])* - Descriptors and performance indexes.

- **Table V.** *Numerical Assessment (Test Case 1 - “Trento Nord”;  $f = 3.5$  [GHz])* - Coverage improvement statistics.
- **Table VI.** *Numerical Assessment (Test Case 2 - “San Martino”;  $f = 3.5$  [GHz])* - BTS radiation features.
- **Table VII.** *Numerical Assessment (Test Case 2 - “San Martino”;  $f = 3.5$  [GHz])* - Descriptors and performance indexes.
- **Table VIII.** *Numerical Assessment (Test Case 2 - “San Martino”;  $f = 3.5$  [GHz])* - Coverage improvement statistics.
- **Table IX.** *Numerical Assessment (Test Case 2 - “San Martino”;  $f = 3.5$  [GHz])* - Coverage improvement statistics.



(a)



(b)

Fig. 1 - A. Benoni et al., "A Planning Strategy for ..."

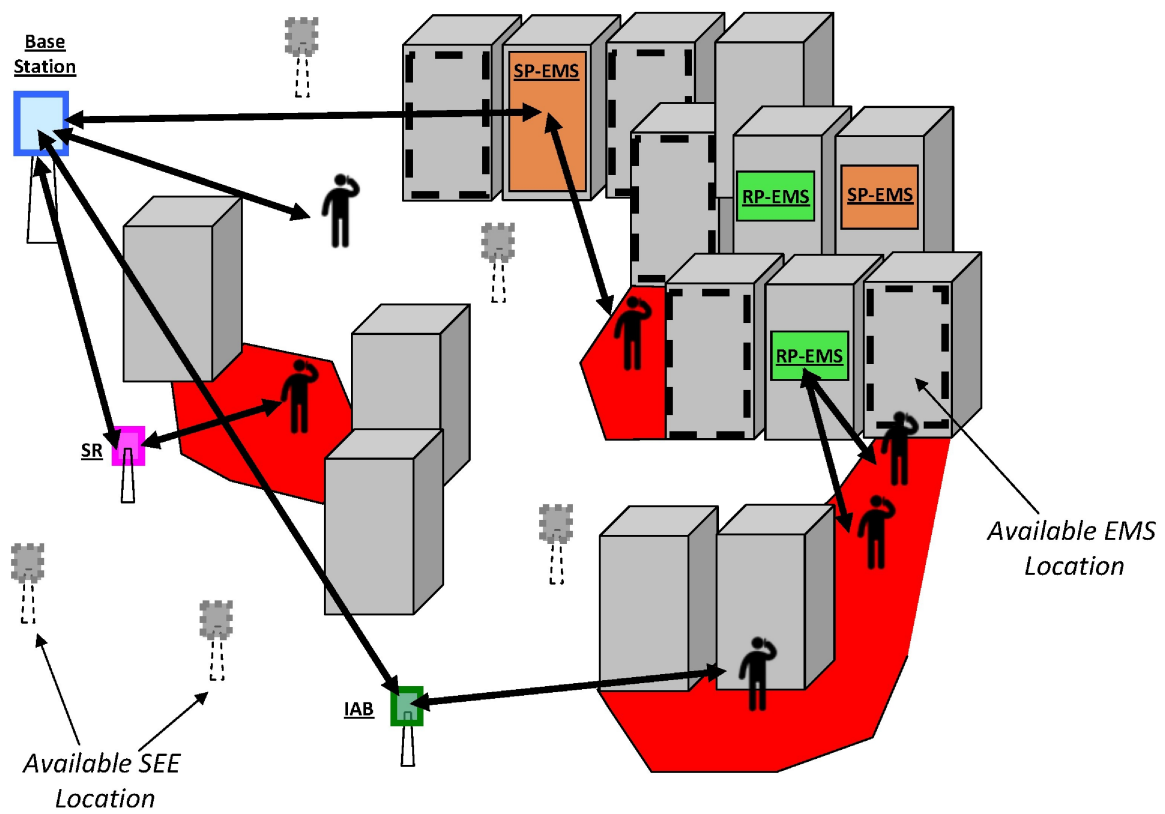


**Fig. 2 - A. Benoni et al., “A Planning Strategy for ...”**

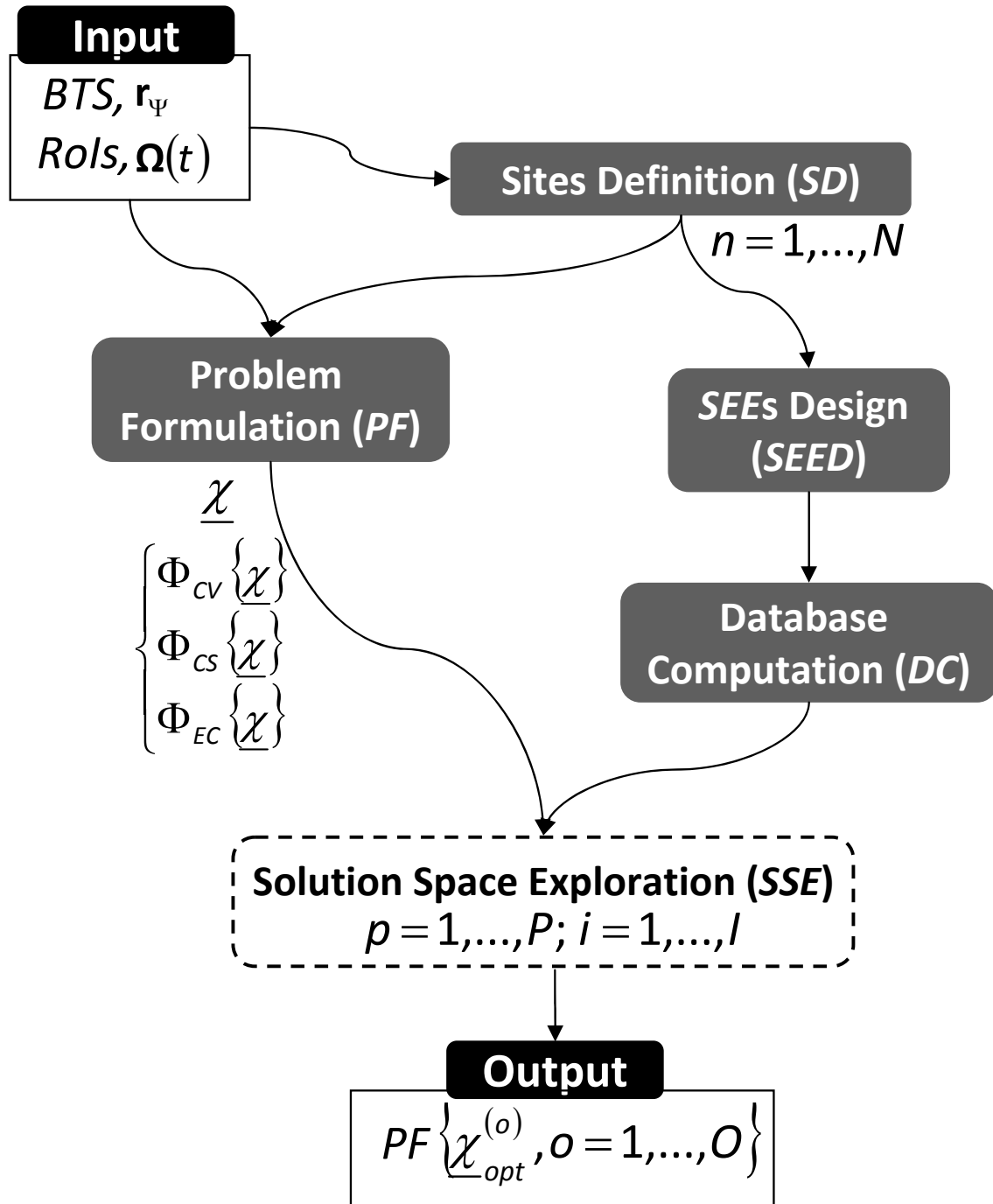
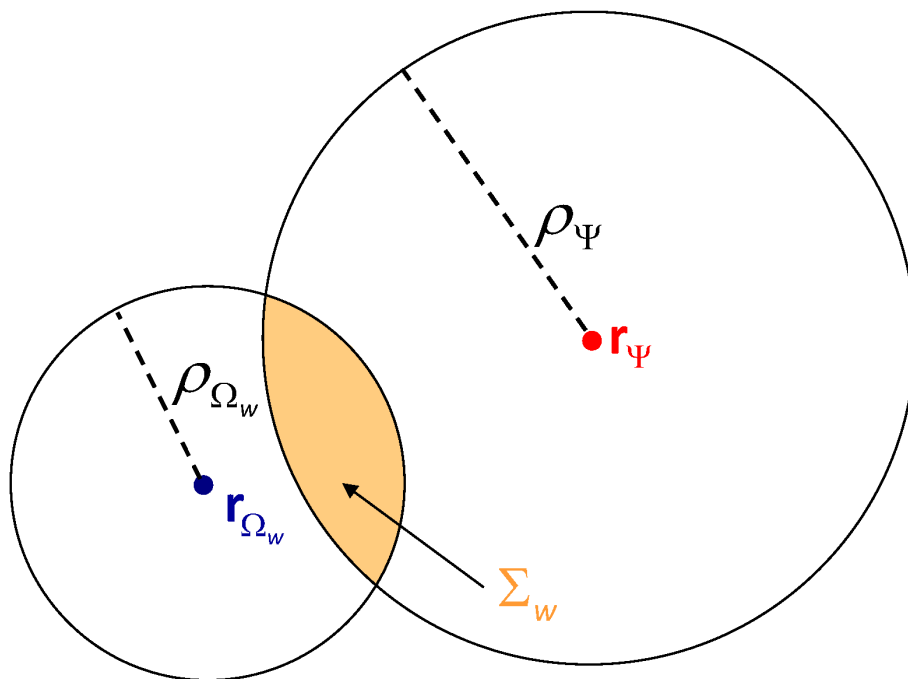
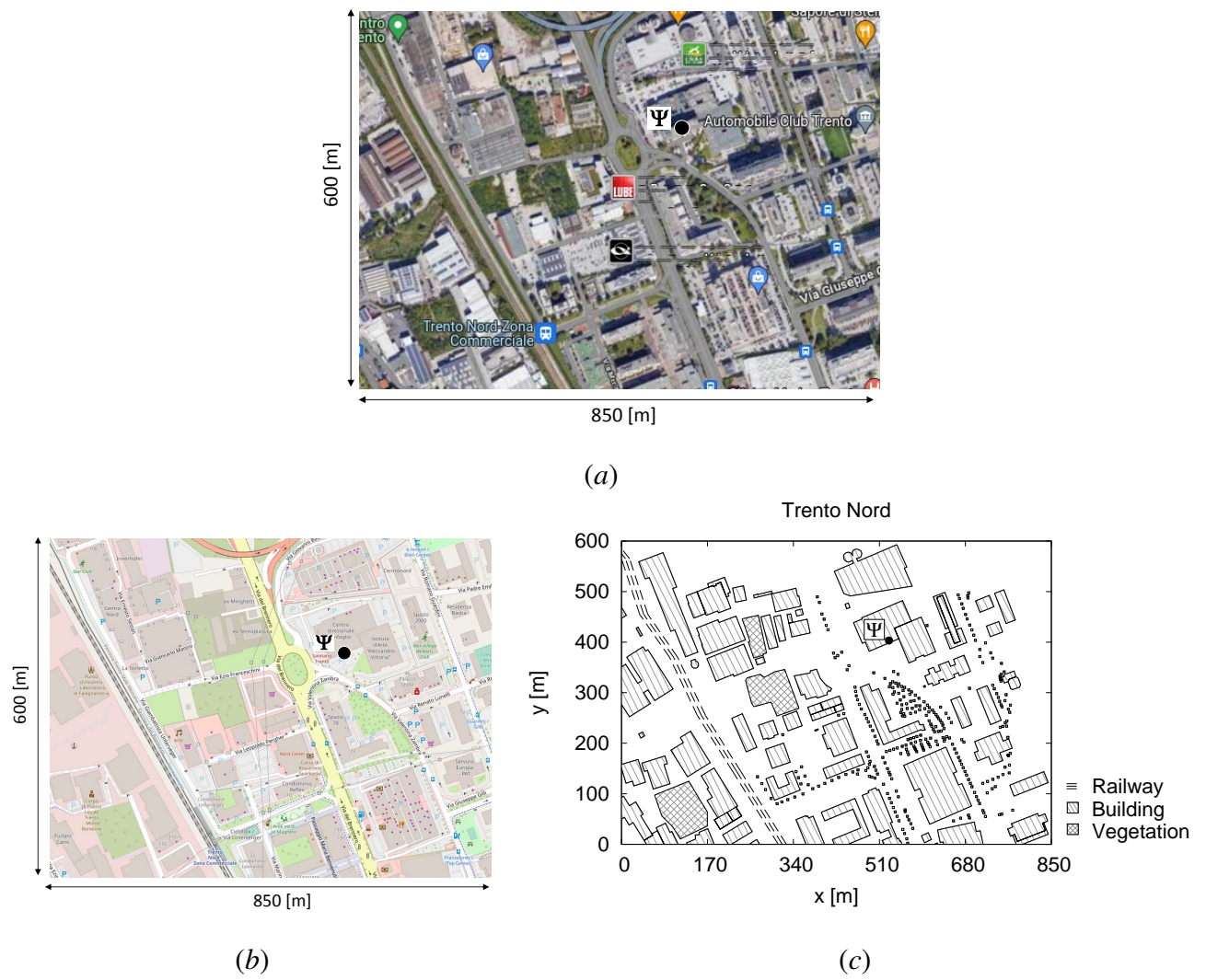


Fig. 3 - A. Benoni et al., “A Planning Strategy for ...”





**Fig. 5 - A. Benoni et al., “A Planning Strategy for ...”**



**Fig. 6 - A. Benoni et al., “A Planning Strategy for ...”**

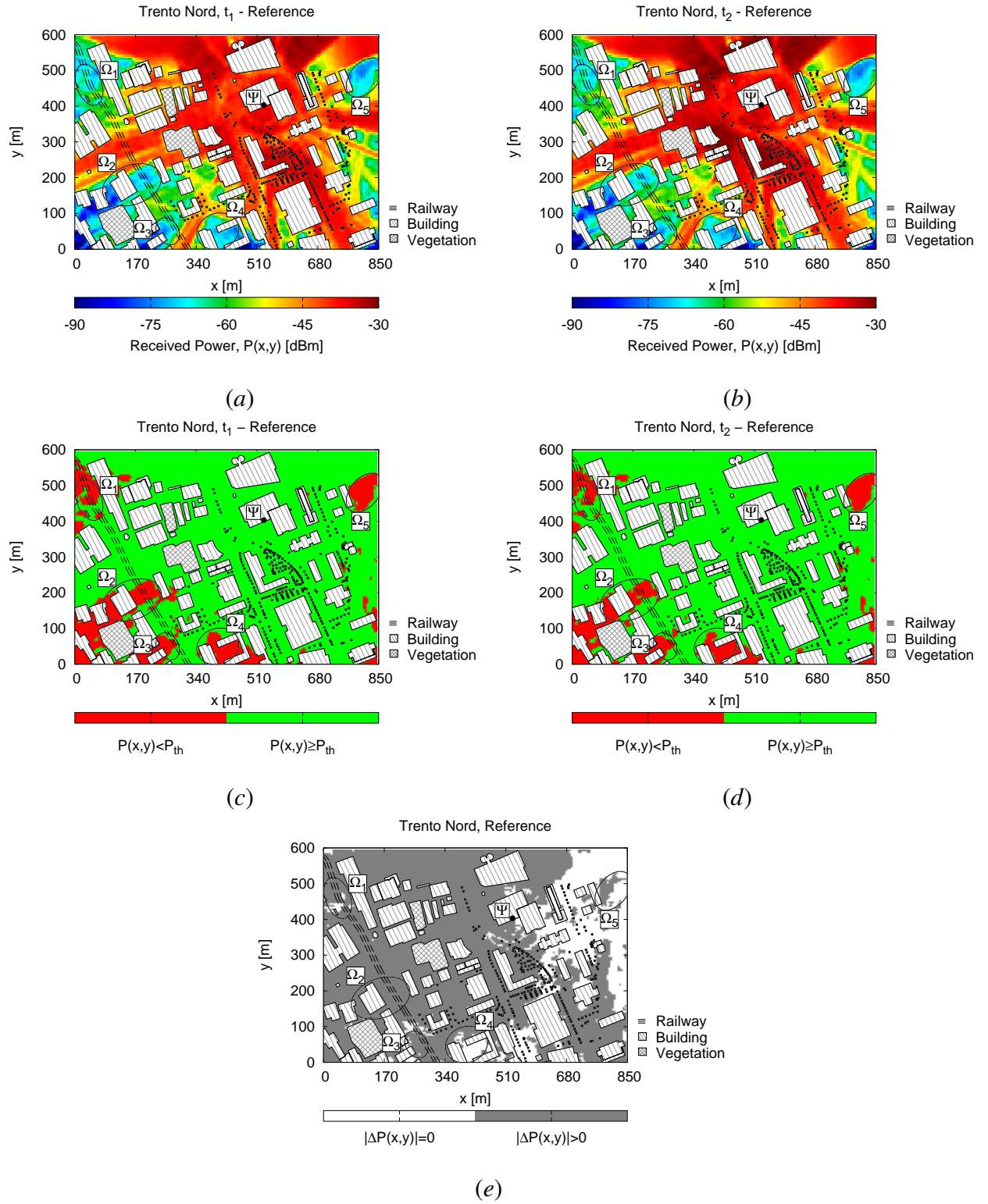


**Fig. 7 - A. Benoni et al., “A Planning Strategy for ...”**

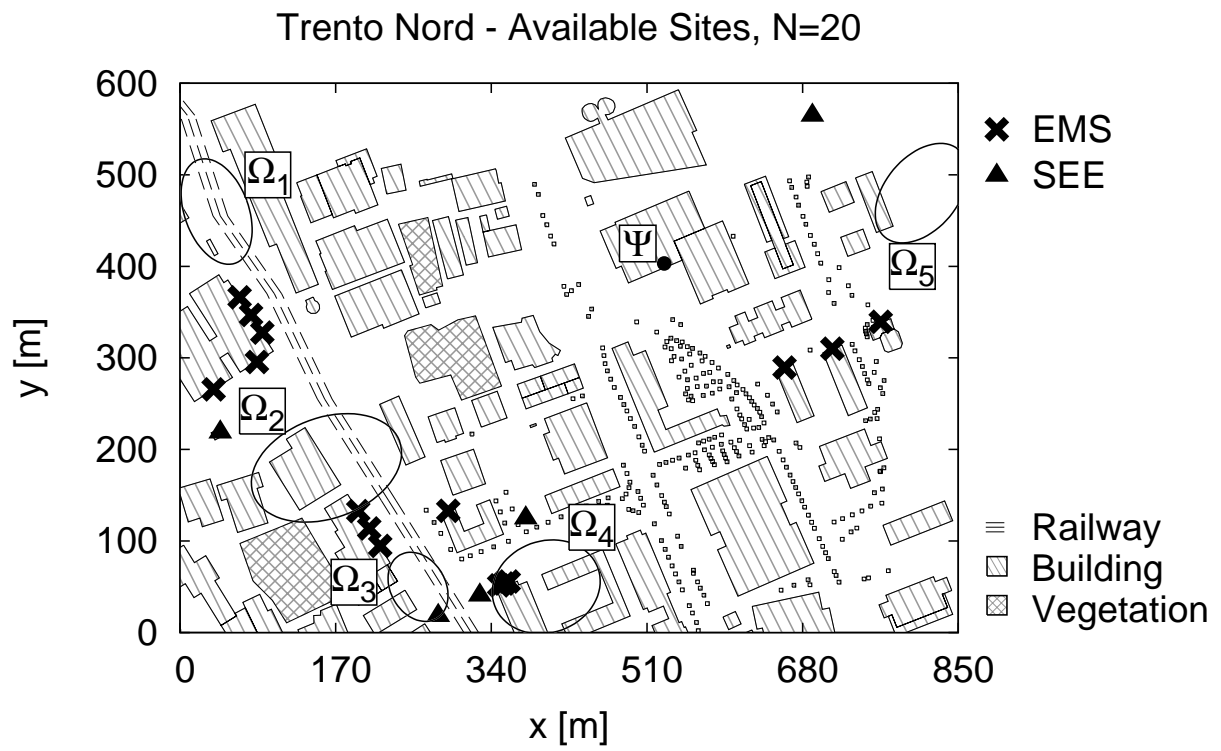
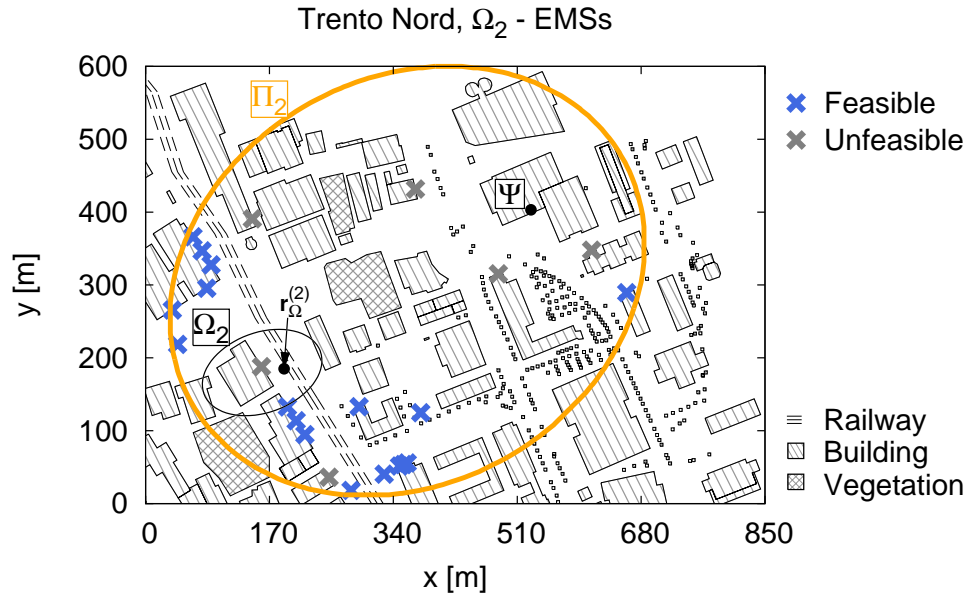
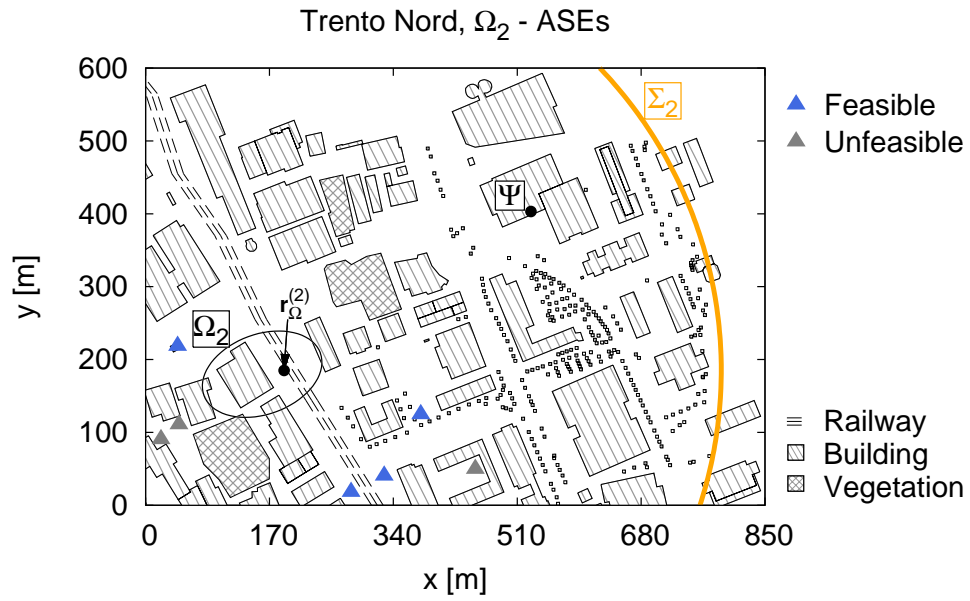


Fig. 8 - A. Benoni et al., “A Planning Strategy for ...”



(a)



(b)

**Fig. 9 - A. Benoni et al., “A Planning Strategy for ...”**

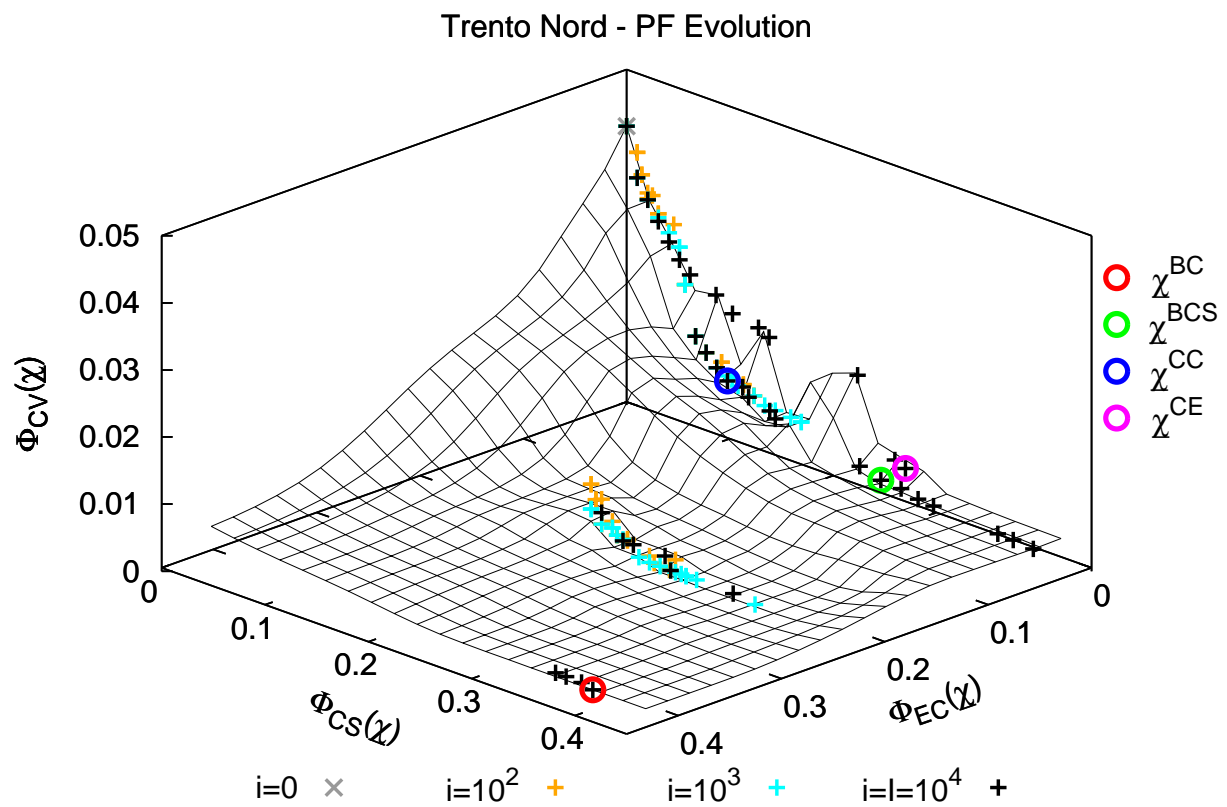
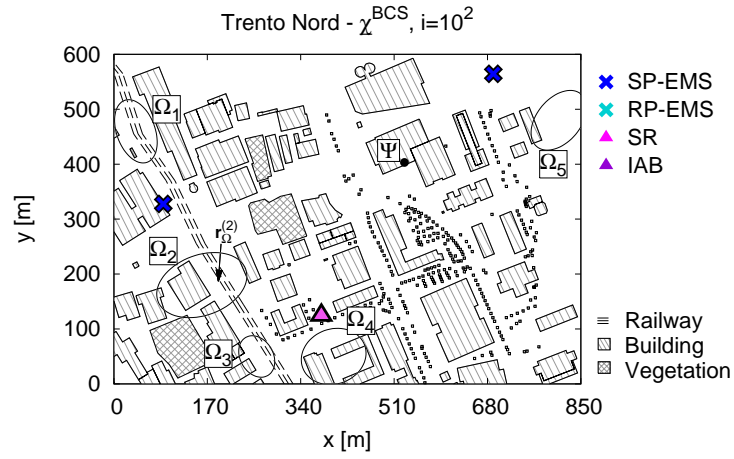
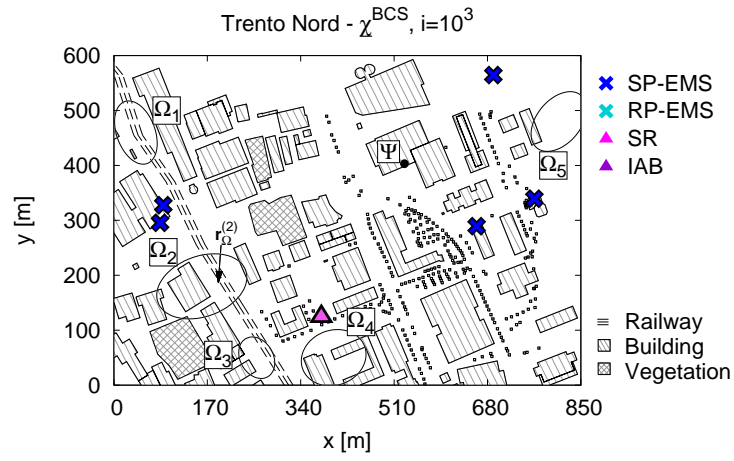


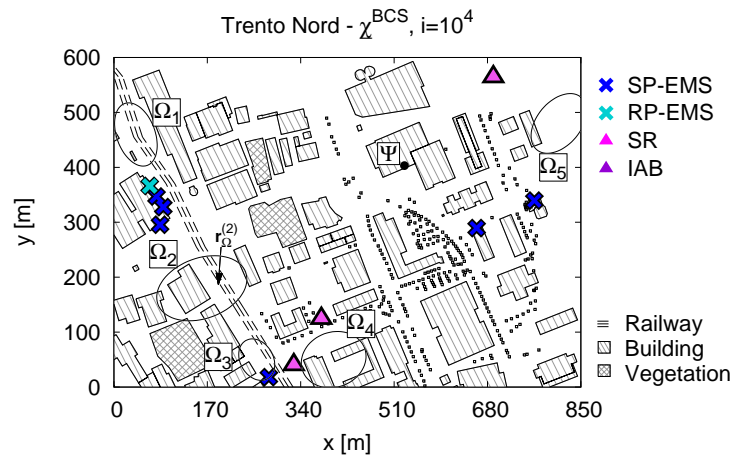
**Fig. 10** - A. Benoni et al., "A Planning Strategy for ..."



(a)



(b)



(c)

**Fig. 11 - A. Benoni et al., “A Planning Strategy for ...”**

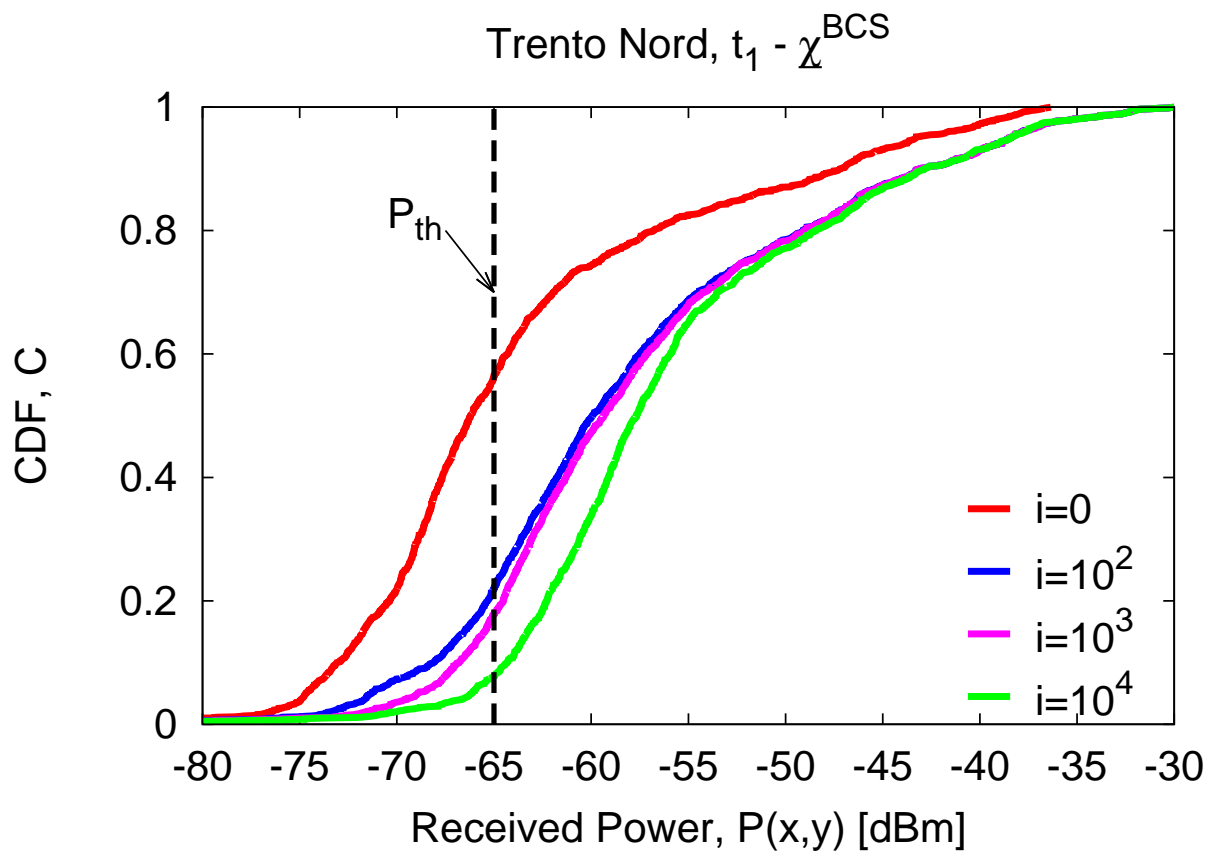


**Fig. 12** - A. Benoni et al., “A Planning Strategy for ...”

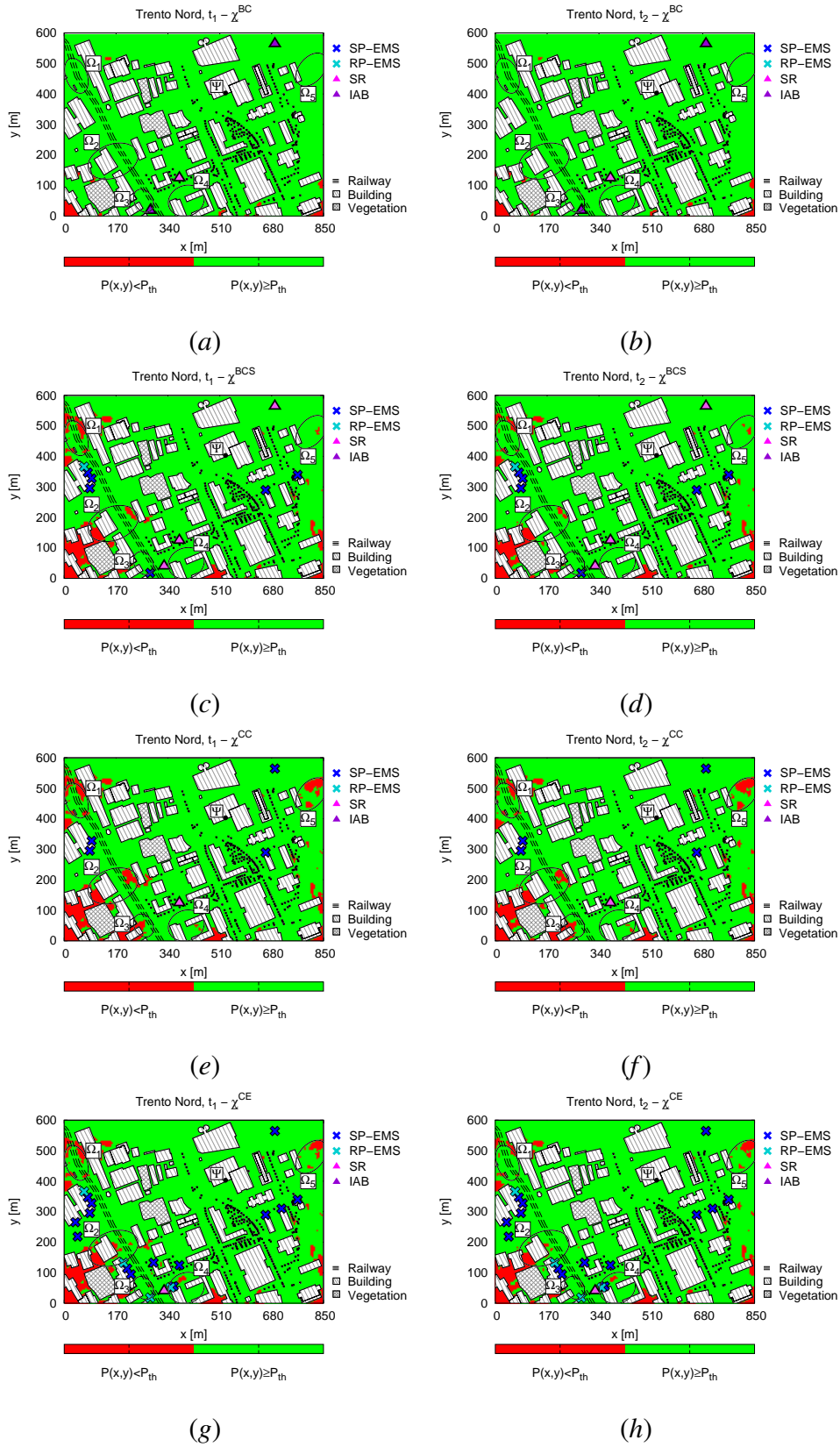
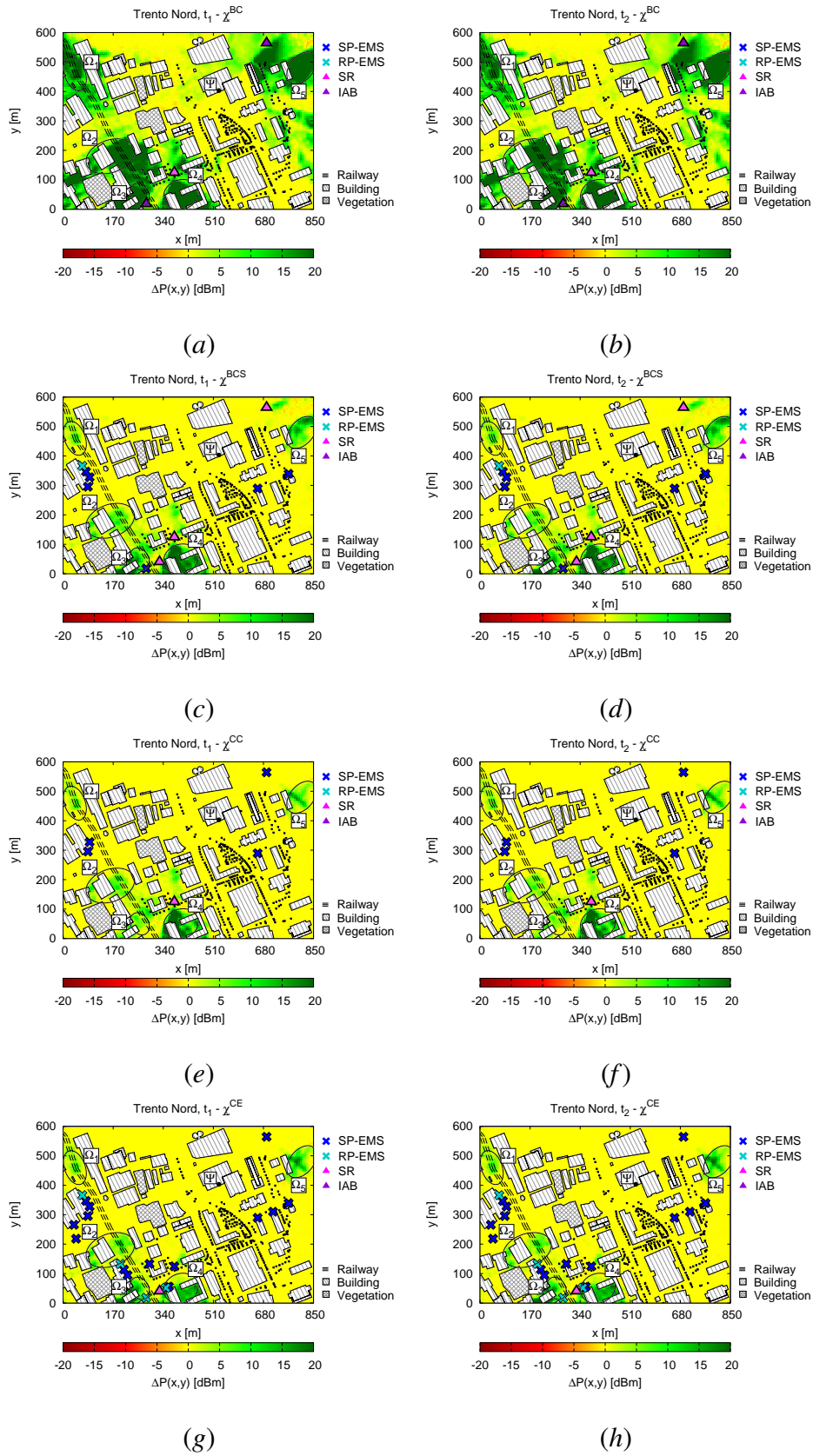
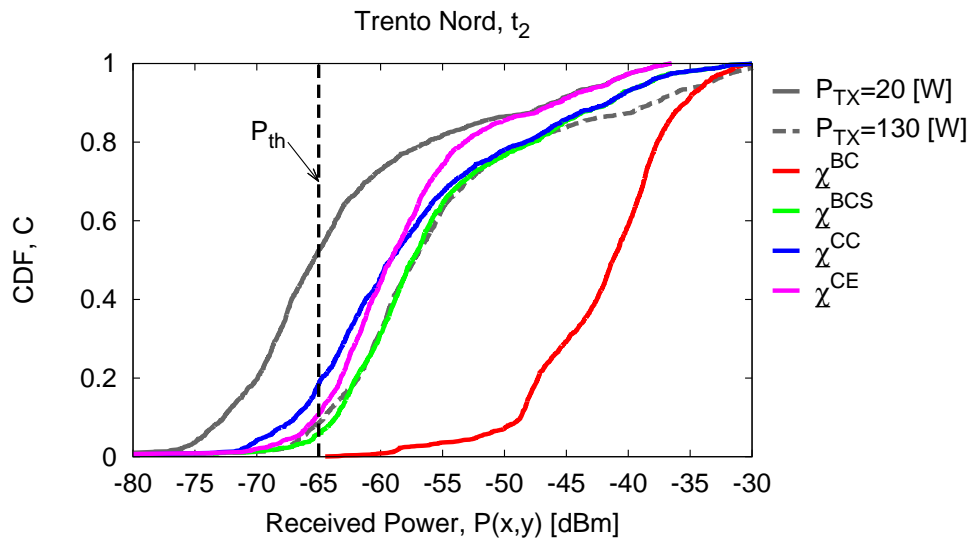
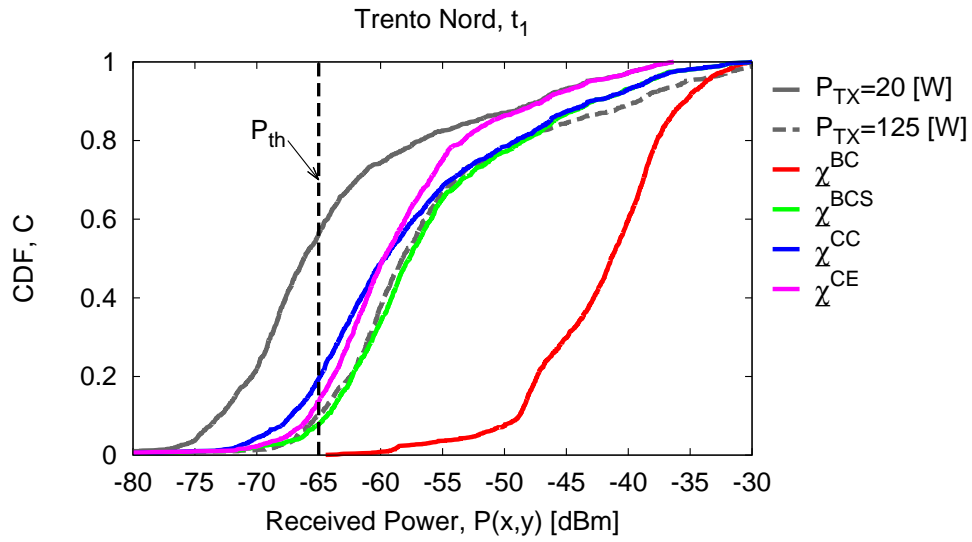


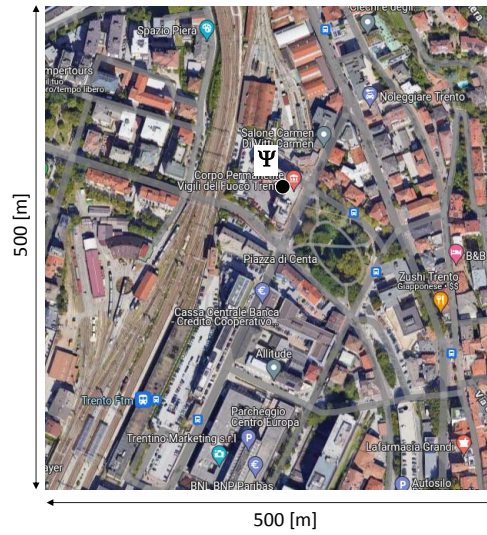
Fig. 13 - A. Benoni et al., “A Planning Strategy for ...”



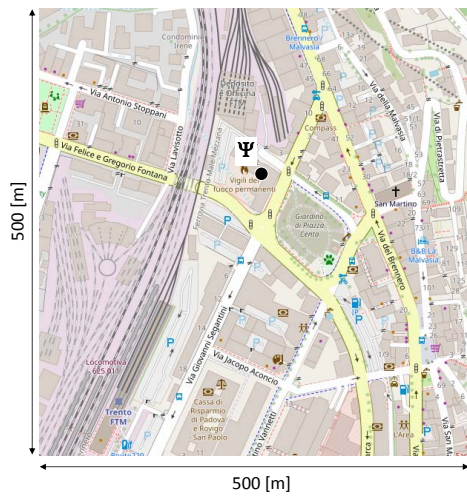
**Fig. 14 - A. Benoni et al., “A Planning Strategy for ...”**



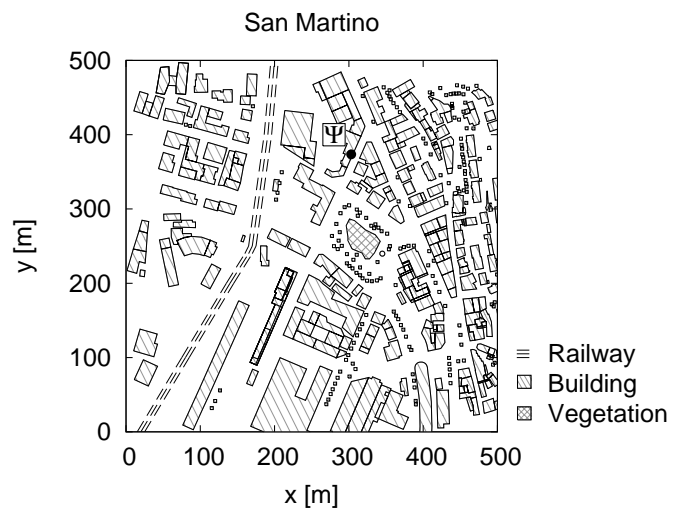
**Fig. 15** - A. Benoni et al., “A Planning Strategy for ...”



(a)



(b)



(c)

**Fig. 16 - A. Benoni et al., “A Planning Strategy for ...”**

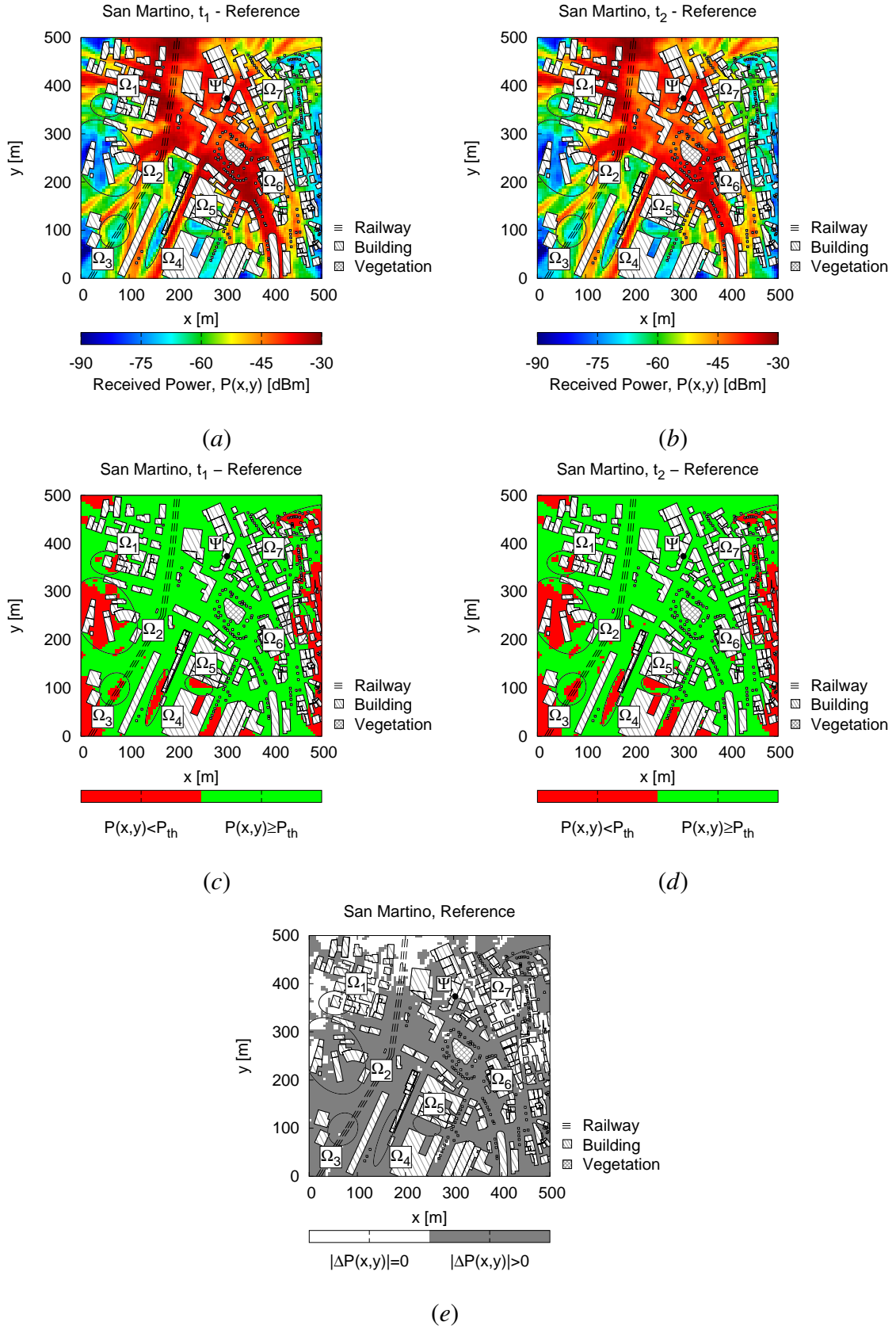


**Fig. 17 - A. Benoni et al., “A Planning Strategy for ...”**

# San Martino - Available Sites, N=25

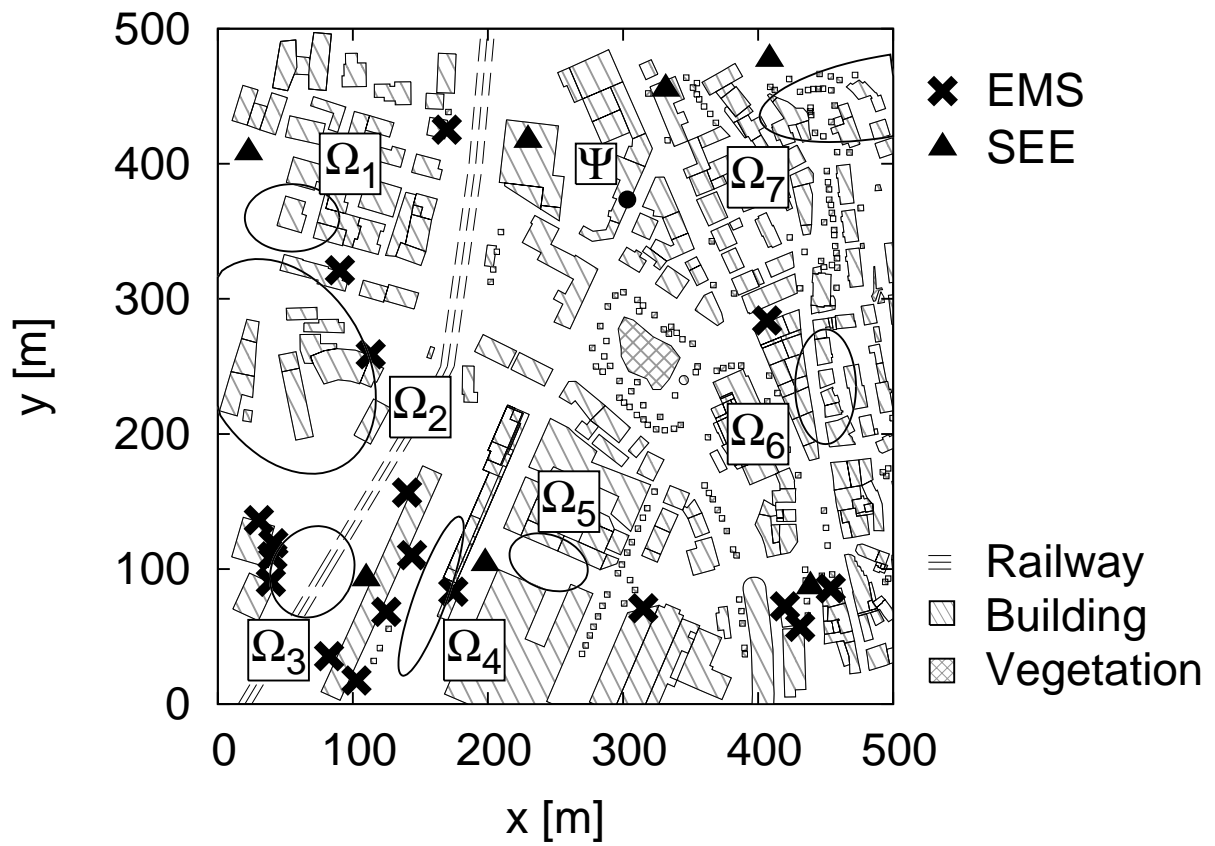
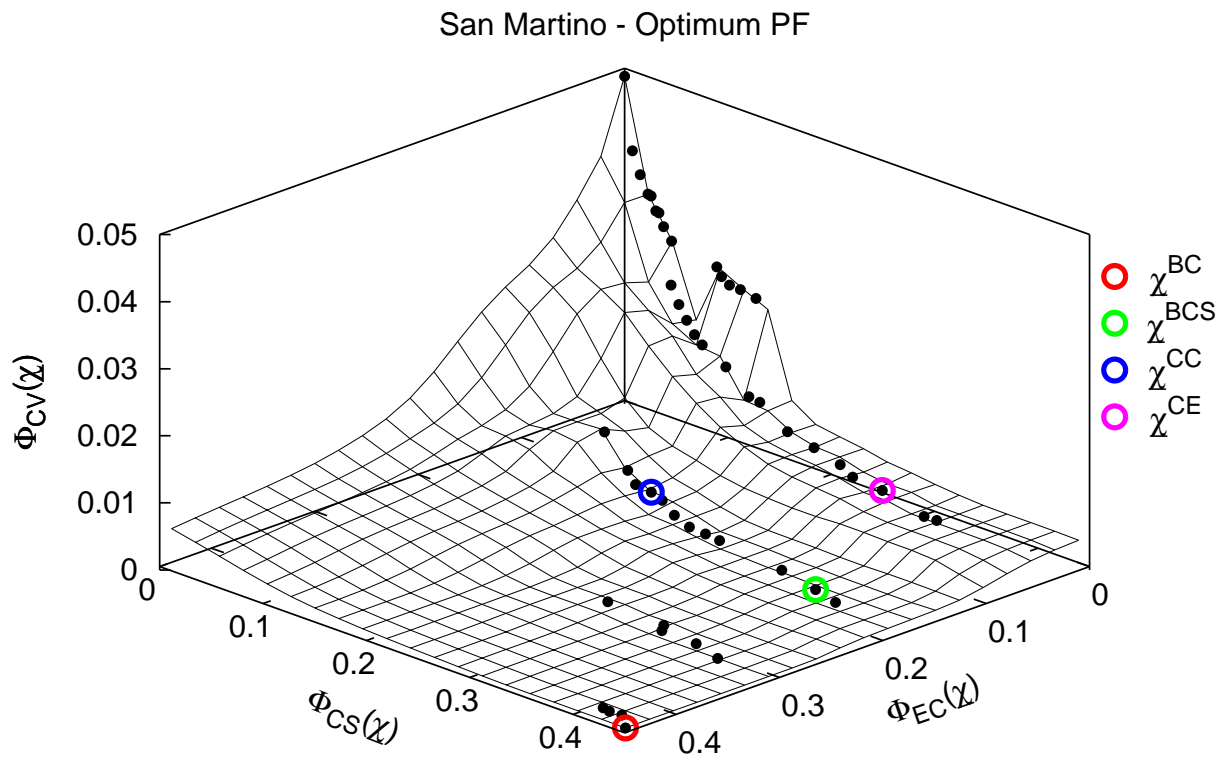
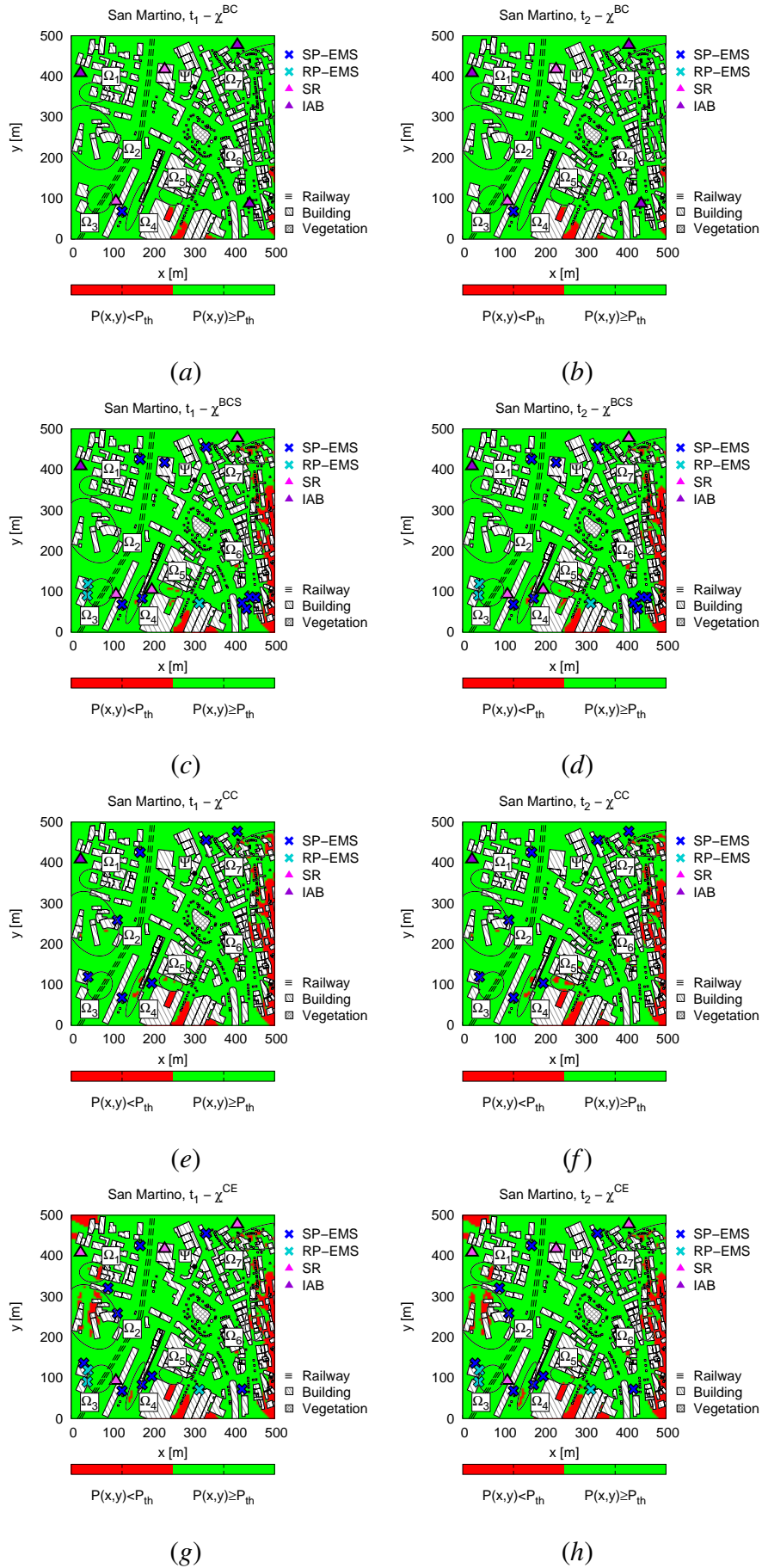


Fig. 18 - A. Benoni et al., “A Planning Strategy for ...”



**Fig. 19** - A. Benoni et al., “A Planning Strategy for ...”



**Fig. 20 - A. Benoni et al., “A Planning Strategy for ...”**

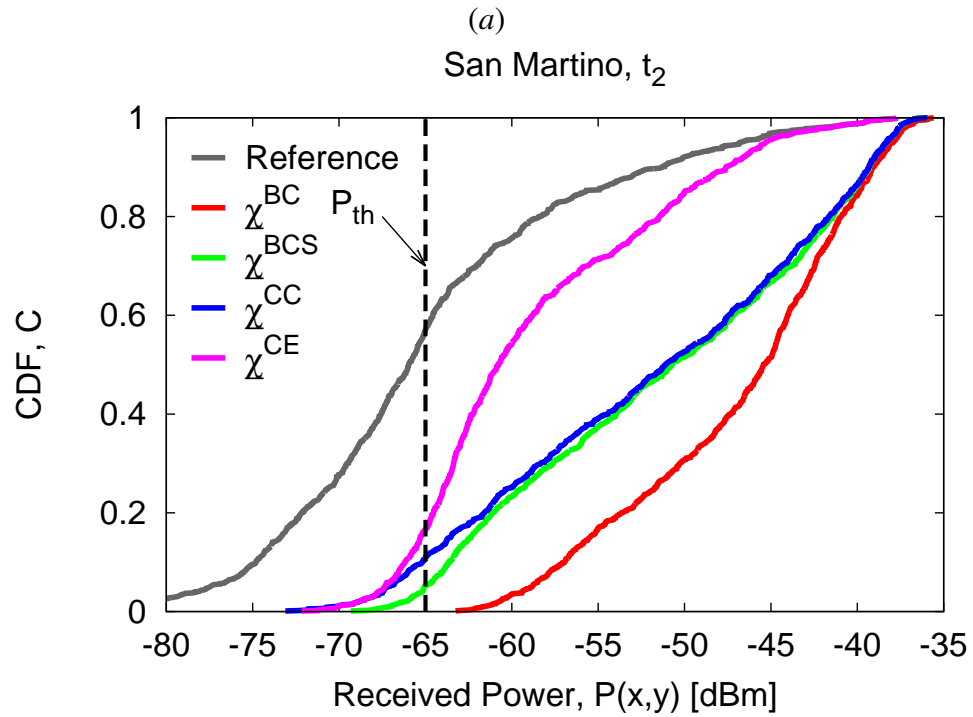
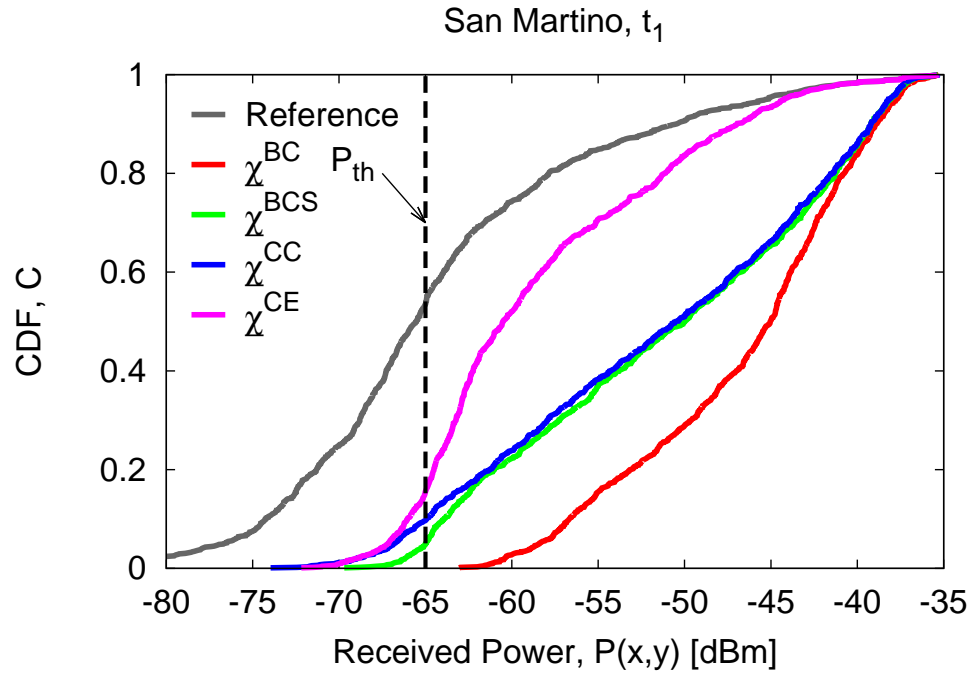


**Fig. 21** - A. Benoni et al., “A Planning Strategy for ...”

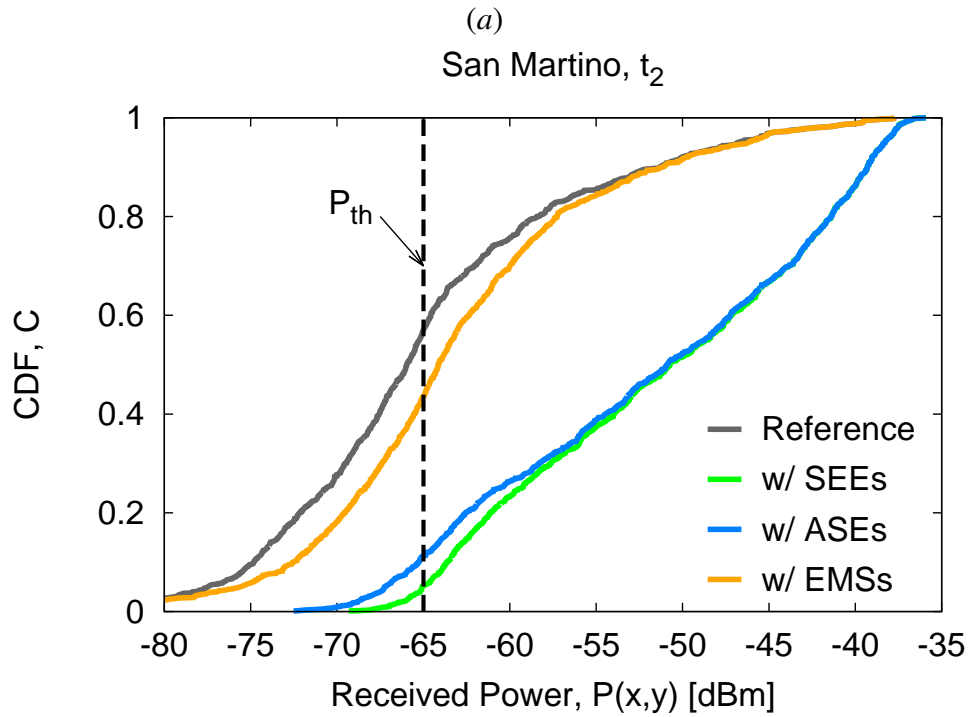
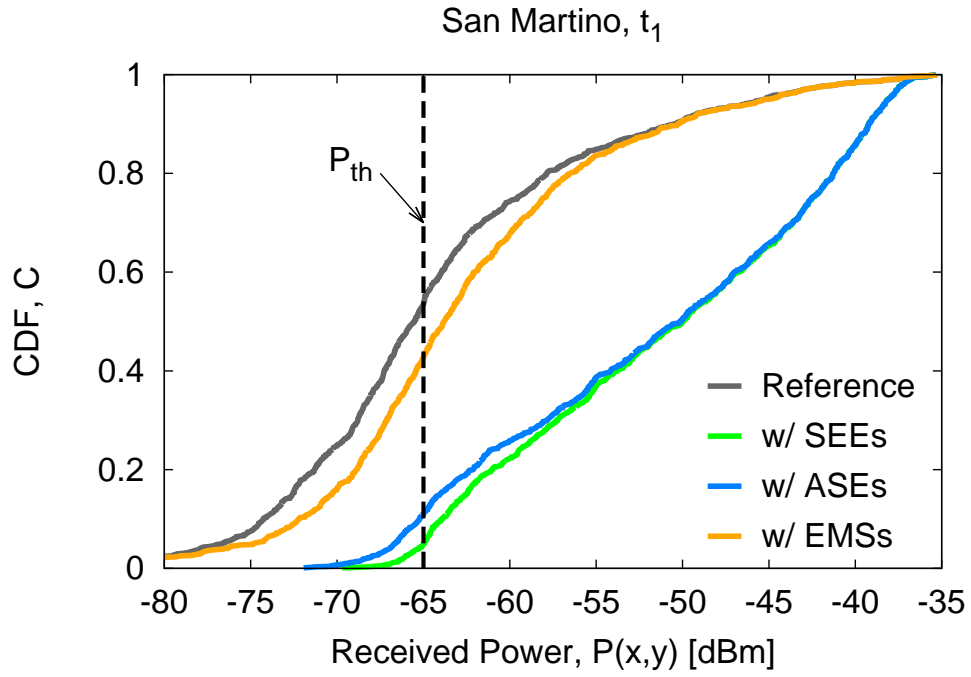


**Fig. 22 - A. Benoni et al., “A Planning Strategy for ...”**

<i>SEE</i>	$\mathcal{P}_s$ [dBm]	$\xi_s$ [\$]	$\nu_s$ [W]
<i>SP-EMS</i>	—	500 (*)	0
<i>RP-EMS</i>	—	750 (*)	$< 2$
<i>SR</i>	24	3000	$\sim 20$
<i>IAB</i>	33	7500	$\leq 350$

(\*) Over-estimation (significantly reduced in a mass-market production)

**Tab. I - A. Benoni et al., “A Planning Strategy for ...”**

<b><i>BTS Sector, <math>v</math></i></b>	<b>Azimuth</b>		<b>Downtilt</b>		<b>TX Power</b>	
	$\Delta\phi_{\Psi}$ [deg]		$\Delta\vartheta_{\Psi}$ [deg]		$\mathcal{P}_{TX}$ [W]	
	$t_1$	$t_2$	$t_1$	$t_2$	$t_1$	$t_2$
1	60	60	2	2	20	20
2	190	200	2	2	20	20
3	330	330	2	4	20	20

**Tab. II - A. Benoni et al., “A Planning Strategy for ...”**

	$\Lambda(\Omega_w(t) \underline{0})$ [m <sup>2</sup> ]		$\Lambda(\Omega_w(t) \underline{\chi}^{BC})$ [m <sup>2</sup> ]		$\Lambda(\Omega_w(t) \underline{\chi}^{BCS})$ [m <sup>2</sup> ]		$\Lambda(\Omega_w(t) \underline{\chi}^{CC})$ [m <sup>2</sup> ]		$\Lambda(\Omega_w(t) \underline{\chi}^{CE})$ [m <sup>2</sup> ]	
$w$	$t_1$	$t_2$	$t_1$	$t_2$	$t_1$	$t_2$	$t_1$	$t_2$	$t_1$	$t_2$
1	2750	2375	0	0	975	425	1125	825	975	425
2	4900	4075	0	0	1125	850	1700	1400	1525	975
3	2550	2525	0	0	0	0	1175	1050	75	25
4	5125	4875	0	0	525	525	725	800	975	850
5	5425	5450	0	0	200	325	2425	2700	1475	1650

**Tab. III - A. Benoni et al., “A Planning Strategy for ...”**

<i>SEME Solution</i>	$\Phi_{CV}(\underline{\chi})$	$\Phi_{CS}(\underline{\chi})$	$\Phi_{EC}(\underline{\chi})$	#SEEs	#SP-EMSs	#RP-EMSs	#SRs	#IABs	$\xi$ [\$]	$\nu$ [W]
<i>BC</i>	0.0	$3.69 \times 10^{-1}$	$4.01 \times 10^{-1}$	3	0	0	1	2	18000	720
<i>BCS</i>	$4.02 \times 10^{-3}$	$2.61 \times 10^{-1}$	$1.53 \times 10^{-2}$	9	6	1	3	0	6750	62
<i>CC</i>	$9.52 \times 10^{-3}$	$1.02 \times 10^{-1}$	$4.96 \times 10^{-3}$	5	4	0	1	0	5000	20
<i>CE</i>	$6.16 \times 10^{-3}$	$2.77 \times 10^{-1}$	$1.54 \times 10^{-3}$	20	15	4	1	0	13500	20

**Tab. IV - A. Benoni et al., “A Planning Strategy for ...”**

		$\Delta\mathcal{P}_{\min}[\text{dB}]$		$\Delta\mathcal{P}_{\max}[\text{dB}]$		$\Delta\mathcal{P}_{\text{avg}}[\text{dB}]$		$\Delta\Omega_w(t) [\%]$	
$w$	<b><i>SEME Solution</i></b>	$t_1$	$t_2$	$t_1$	$t_2$	$t_1$	$t_2$	$t_1$	$t_2$
1	<i>BC</i>	5.7	5.3	24.4	23.9	16.7	15.9	100	100
2	<i>BC</i>	-0.5	-0.6	36.2	34.5	21.6	20.2	100	100
3	<i>BC</i>	4.1	3.6	33.4	32.6	20.0	19.3	100	100
4	<i>BC</i>	0.2	0.1	49.2	47.7	22.3	21.9	100	100
5	<i>BC</i>	-1.4	-1.3	40.1	40.7	23.3	23.7	100	100
1	<i>BCS</i>	-0.1	-0.3	10.6	10.9	3.3	3.7	64.5	82.1
2	<i>BCS</i>	0.0	0.0	12.4	11.4	4.9	4.2	77.1	79.1
3	<i>BCS</i>	0.3	0.2	21.0	20.8	8.0	7.5	100	100
4	<i>BCS</i>	-0.2	-0.4	36.5	35.7	14.7	14.4	89.8	89.2
5	<i>BCS</i>	-1.3	-1.4	19.9	19.8	6.3	6.5	96.3	94.1
1	<i>CC</i>	-0.7	-0.7	10.5	10.8	2.8	2.9	59.1	65.3
2	<i>CC</i>	0.0	-0.2	11.9	11.5	4.3	3.6	65.3	65.6
3	<i>CC</i>	-1.0	-1.2	13.3	13.9	4.8	4.4	53.9	58.4
4	<i>CC</i>	-0.4	-0.4	36.4	35.7	13.2	12.8	85.6	83.6
5	<i>CC</i>	-0.8	-0.7	20.0	21.3	4.0	4.2	55.3	50.5
1	<i>CE</i>	0.0	-0.2	10.5	13.7	3.3	3.6	64.5	82.1
2	<i>CE</i>	0.0	0.0	15.5	21.0	4.3	3.8	68.9	76.1
3	<i>CE</i>	-0.2	-0.3	21.3	20.1	5.6	5.1	97.1	99.0
4	<i>CE</i>	-0.6	-0.5	20.0	20.0	7.1	7.1	81.0	82.6
5	<i>CE</i>	-0.7	-0.7	10.8	21.4	5.2	5.4	72.8	69.7

**Tab. V - A. Benoni et al., “A Planning Strategy for ...”**

<b><i>BTS Sector, <math>v</math></i></b>	<b>Azimuth</b>		<b>Downtilt</b>		<b>TX Power</b>	
	$\Delta\phi_{\Psi}$ [deg]		$\Delta\vartheta_{\Psi}$ [deg]		$\mathcal{P}_{TX}$ [W]	
	$t_1$	$t_2$	$t_1$	$t_2$	$t_1$	$t_2$
1	0	5	2	3	20	20
2	120	115	2	2	20	20
3	240	250	2	1	20	20

**Tab. VI - A. Benoni et *al.*, “A Planning Strategy for ...”**

<i>SEME Solution</i>	$\Phi_{CV}(\underline{\chi})$	$\Phi_{CS}(\underline{\chi})$	$\Phi_{EC}(\underline{\chi})$	#SEEs	#SP-EMSs	#RP-EMSs	#SRs	#IABs	$\xi$ [\$]	$\nu$ [W]
<i>BC</i>	0.0	$4.39 \times 10^{-1}$	$4.38 \times 10^{-1}$	6	1	0	2	3	33500	1090
<i>BCS</i>	$9.07 \times 10^{-4}$	$3.52 \times 10^{-1}$	$1.67 \times 10^{-1}$	16	9	3	3	1	23250	416
<i>CC</i>	$3.74 \times 10^{-3}$	$1.67 \times 10^{-1}$	$1.41 \times 10^{-1}$	8	7	0	0	1	11000	350
<i>CE</i>	$4.61 \times 10^{-3}$	$2.84 \times 10^{-1}$	$3.46 \times 10^{-2}$	15	9	3	3	0	15750	66

**Tab. VII - A. Benoni et al., “A Planning Strategy for ...”**

		$\Delta\mathcal{P}_{\min}[\text{dB}]$		$\Delta\mathcal{P}_{\max}[\text{dB}]$		$\Delta\mathcal{P}_{\text{avg}}[\text{dB}]$		$\Delta\Omega_w(t) [\%]$	
$w$	<b>SEME Solution</b>	$t_1$	$t_2$	$t_1$	$t_2$	$t_1$	$t_2$	$t_1$	$t_2$
1	<i>BC</i>	12.5	12.8	28.4	28.3	20.7	20.9	100	100
2	<i>BC</i>	-4.5	-0.3	30.9	30.6	21.7	22.3	100	100
3	<i>BC</i>	6.7	7.4	25.5	26.3	16.7	17.6	100	100
4	<i>BC</i>	-0.7	-0.7	20.2	21.0	5.6	6.2	100	100
5	<i>BC</i>	6.3	7.5	20.5	22.8	15.1	17.0	100	100
6	<i>BC</i>	4.7	5.1	31.1	31.7	15.8	16.3	100	100
7	<i>BC</i>	3.5	2.7	31.9	30.8	19.8	18.8	100	100
1	<i>BCS</i>	12.5	12.8	28.4	28.3	20.7	20.9	100	100
2	<i>BCS</i>	0.0	0.0	30.9	30.6	20.9	21.5	100	100
3	<i>BCS</i>	4.4	5.1	25.6	26.5	14.7	15.6	100	100
4	<i>BCS</i>	-1.1	-1.5	18.1	18.7	30.4	5.7	94.5	89.2
5	<i>BCS</i>	0.1	1.4	15.4	17.3	5.3	8.1	78.3	92.8
6	<i>BCS</i>	-0.1	-0.1	12.0	11.1	2.5	2.3	61.3	41.0
7	<i>BCS</i>	-0.3	-0.2	14.1	13.1	3.4	3.0	71.9	74.6
1	<i>CC</i>	12.5	12.8	28.4	28.3	20.8	20.8	100	100
2	<i>CC</i>	0.0	0.0	30.9	30.6	21.0	21.5	98.4	98.5
3	<i>CC</i>	0.8	1.4	24.3	24.7	12.3	13.2	96.6	97.7
4	<i>CC</i>	-0.7	-0.6	17.6	18.1	4.3	4.8	81.8	81.5
5	<i>CC</i>	-0.1	0.0	15.5	15.8	5.4	5.7	82.6	53.5
6	<i>CC</i>	-0.2	-0.2	0.5	0.5	0.0	0.0	3.2	5.1
7	<i>CC</i>	-0.3	-0.4	20.3	18.8	3.0	2.5	51.7	49.2
1	<i>CE</i>	0.3	0.2	6.5	6.2	2.1	20.5	28	33.3
2	<i>CE</i>	-1.5	-1.5	25.6	25.2	7.0	7.4	72.2	71.3
3	<i>CE</i>	2.3	2.8	23.7	24.6	12.9	1.4	100	100
4	<i>CE</i>	-0.5	-0.5	20.4	21.3	4.2	4.7	87.3	81.5
5	<i>CE</i>	0.6	1.9	18.9	20.4	8.1	9.9	100	96.4
6	<i>CE</i>	-0.3	-0.4	10.7	9.5	1.4	1.2	19.3	20.5
7	<i>CE</i>	-0.1	0.0	14.0	13.0	3.4	3.0	69.6	73.2

**Tab. VIII - A. Benoni et al., “A Planning Strategy for ...”**

		$\Delta\mathcal{P}_{\min}[\text{dB}]$		$\Delta\mathcal{P}_{\max}[\text{dB}]$		$\Delta\mathcal{P}_{\text{avg}}[\text{dB}]$		$\Delta\Omega_w(t) [\%]$	
$w$	Configuration	$t_1$	$t_2$	$t_1$	$t_2$	$t_1$	$t_2$	$t_1$	$t_2$
1	w/ <i>SEEs</i>	12.5	12.8	28.4	28.3	20.7	20.9	100	100
2	w/ <i>SEEs</i>	0.0	0.0	30.9	30.6	20.9	21.5	100	100
3	w/ <i>SEEs</i>	4.4	5.1	25.6	26.5	14.7	15.6	100	100
4	w/ <i>SEEs</i>	-1.1	-1.5	18.1	18.7	30.4	5.7	94.5	89.2
5	w/ <i>SEEs</i>	0.1	1.4	15.4	17.3	5.3	8.1	78.3	92.8
6	w/ <i>SEEs</i>	-0.1	-0.1	12.0	11.1	2.5	2.3	61.3	41.0
7	w/ <i>SEEs</i>	-0.3	-0.2	14.1	13.1	3.4	3.0	71.9	74.6
1	w/ <i>ASEs</i>	12.5	12.8	28.4	28.3	20.7	20.8	100	100
2	w/ <i>ASEs</i>	-0.1	0.0	30.9	30.5	20.9	21.5	100	100
3	w/ <i>ASEs</i>	3.5	4.0	25.3	26.2	14.2	15.1	100	100
4	w/ <i>ASEs</i>	-1.2	-1.6	15.0	16.3	3.8	4.4	56.3	61.5
5	w/ <i>ASEs</i>	0.3	0.8	7.1	8.7	3.0	3.9	43.5	28.6
6	w/ <i>ASEs</i>	-0.3	-0.2	0.4	0.5	0.0	0.0	-6.45	0.0
7	w/ <i>ASEs</i>	-0.3	-0.3	14.4	13.2	3.16	2.8	59.6	67.6
1	w/ <i>EMSs</i>	-0.3	-0.7	0.3	0.4	0.0	0.0	-4.0	0.0
2	w/ <i>EMSs</i>	-1.4	-0.2	8.4	10.3	1.2	1.1	5.0	2.6
3	w/ <i>EMSs</i>	-0.6	-0.8	9.4	10.5	3.4	3.6	90	88.6
4	w/ <i>EMSs</i>	-0.1	-0.7	17.4	18.0	2.4	2.8	49.1	55.4
5	w/ <i>EMSs</i>	0.5	0.9	14.0	15.6	4.0	6.9	56.5	75.0
6	w/ <i>EMSs</i>	-0.1	-0.1	12.1	11.2	2.4	2.2	51.6	41.0
7	w/ <i>EMSs</i>	-0.7	-0.6	3.7	2.8	0.6	0.5	10.1	12.7

**Tab. IX - A. Benoni et al., “A Planning Strategy for ...”**